The Meteoritical Society

Meteoritics & Planetary Science 43, Nr 12, 1955–1977 (2008)
Abstract available online at http://meteoritics.org

Mid-sized complex crater formation in mixed crystalline-sedimentary targets: Insight from modeling and observation

G. S. COLLINS[1*], T. KENKMANN[2], G. R. OSINSKI[3], and K. WÜNNEMANN[2]

[1]IARC, Department of Earth Science and Engineering, Imperial College London, London, SW7 2AZ, United Kingdom
[2]Museum für Naturkunde, Humboldt-Universität Berlin, Invalidenstraße 43, 10115 Berlin, Germany
[3]Departments of Earth Science/Physics and Astronomy, University of Western Ontario, 1151 Richmond Street, London, ON, N6A 5B7, Canada
[*]Corresponding author. E-mail: g.collins@imperial.ac.uk

(Received 01 April 2008; revision accepted 21 October 2008)

Abstract–Large impact crater formation is an important geologic process that is not fully understood. The current paradigm for impact crater formation is based on models and observations of impacts in homogeneous targets. Real targets are rarely uniform; for example, the majority of Earth's surface is covered by sedimentary rocks and/or a water layer. The ubiquity of layering across solar system bodies makes it important to understand the effect target properties have on the cratering process. To advance understanding of the mechanics of crater collapse, and the effect of variations in target properties on crater formation, the first "Bridging the Gap" workshop recommended that geological observation and numerical modeling focussed on mid-sized (15–30 km diameter) craters on Earth. These are large enough to be complex; small enough to be mapped, surveyed and modelled at high resolution; and numerous enough for the effects of target properties to be potentially disentangled from the effects of other variables. In this paper, we compare observations and numerical models of three 18–26 km diameter craters formed in different target lithology: Ries, Germany; Haughton, Canada; and El'gygytgyn, Russia. Based on the first-order assumption that the impact energy was the same in all three impacts we performed numerical simulations of each crater to construct a simple quantitative model for mid-sized complex crater formation in a subaerial, mixed crystalline-sedimentary target. We compared our results with interpreted geological profiles of Ries and Haughton, based on detailed new and published geological mapping and published geophysical surveys. Our combined observational and numerical modeling work suggests that the major structural differences between each crater can be explained by the difference in thickness of the pre-impact sedimentary cover in each case. We conclude that the presence of an inner ring at Ries, and not at Haughton, is because basement rocks that are stronger than the overlying sediments are sufficiently close to the surface that they are uplifted and overturned during excavation and remain as an uplifted ring after modification and post-impact erosion. For constant impact energy, transient and final crater diameters increase with increasing sediment thickness.

INTRODUCTION

A phenomenological model for the formation of impact craters in uniform crystalline targets exists, based on decades of geological, geophysical, experimental and theoretical study (Gault et al. 1968; Dence et al. 1977; Grieve et al. 1981; Melosh 1989). An impact excavates a deep, bowl-shaped cavity—the transient crater—that subsequently collapses under gravity to form the final crater morphology. Numerical simulations have verified this model, to a large extent, by reproducing the final crater morphology of many large terrestrial craters (e.g., Ivanov and Deutsch 1999; Collins et al. 2002; Ivanov 2005), and the size morphology progression of lunar impact craters (Wünnemann and Ivanov 2003). Despite the importance of this standard model in a planetary context, many craters in the solar system did not form in a uniform crystalline target. The majority of Earth's surface, for example, is covered by sedimentary rocks and/or a water layer. Target layering exists in many other contexts in the solar system, due to variations in composition and temperature: ice (water) and sediment layers on Mars; brittle and ductile ice or water layers on the icy satellites; regolith

layers on asteroids, comets and other airless bodies; and, at the largest scale, crust over mantle on differentiated planets and satellites. The ubiquity of target layering throughout the solar system makes it important to quantify the effect this has on the cratering process, as evidenced by the number of recent impact modeling studies on this topic (Shuvalov et al. 2002; Shuvalov and Dypvik 2004; Collins and Wünnemann 2005; Ivanov 2005; Wünnemann et al. 2005; Senft and Stewart 2007; Collins et al. 2008; Senft and Stewart 2008).

The termination of crater growth and the degree and nature of subsequent crater collapse is controlled by gravity and the "strength" of the target material (Melosh 1989). In this context, strength means the resistance to shear deformation offered by the target after it has been processed by the shock wave (fractured, heated, and set in motion) and until the major cratering motions have ceased, which we refer to as the "dynamic shear strength." For planetary-scale cratering, impactor size, impact velocity and planetary gravity are the most important factors affecting the size of an impact crater. However, for a specific planetary gravity and a specific impactor size, density, velocity, and trajectory angle to the target surface, the dynamic shear strength of the target can have an important effect on the size, morphology and subsurface structure of an impact crater. Consequently, variations in this dynamic shear strength within a target can have a profound effect on crater formation. The effect of a weak layer overlying a strong layer was investigated experimentally as early as the 1960s, to provide insight into the effect of lunar regolith thickness on small impact crater formation on the moon (Oberbeck and Quaide 1967). Based on small-scale hypervelocity laboratory impact experiments into layered targets, Oberbeck and Quaide (1967) concluded that for a sufficient contrast in layer strength, the morphology of the crater was affected by the stronger underlying layer when the ratio of crater diameter to layer thickness exceeded about 4. Craters with central mounds, flat floors or a small deep crater nested within a shallow outer crater were produced, depending on the relative strength of the target layers and the ratio of crater diameter to weak layer thickness. Oberbeck and Quaide's conclusions were used to correctly estimate lunar regolith thickness before the Apollo missions, using images of small lunar craters, and were reproduced by recent numerical simulations of meter-scale impacts on the lunar surface (Senft and Stewart 2007). Similarly, the "inverted-sombrero" morphology (a broad, shallow outer basin, surrounding a deeper inner basin) characteristic of craters like Mjølnir (Tsikalas et al. 1998) and Chesapeake Bay (Poag et al. 1999) is likely to be a consequence of the sedimentary layer being substantially weaker than the underlying basement (because it is poorly-lithified or water-saturated, for instance). Numerical simulations of these impacts that include a large contrast in strength between the sedimentary and crystalline layers give excellent agreement with interpretations of geophysical data from the craters (Shuvalov and Dypvik 2004; Collins and Wünnemann 2005). The rheological stratification of target rocks also influences the geometry and distribution of major impact-induced shear zones. Strain associated with crater collapse is often concentrated into rheologically soft beds, such as clay or marl layers, which then control further deformation. If the sedimentary target is flat lying this can result in low-angle normal faulting or detachments (Kenkmann et al. 2000). Strain localization along the interface between a strong layer and a weak one could cause a mechanical decoupling of the two layers. This interface could be between basement and sedimentary cover, or within the sedimentary sequence where competent sedimentary rocks, such as limestone, overly weaker sedimentary rocks, such as evaporite lithologies.

Understanding the large-scale, dynamic shear strength of rock during impact is imperative for correctly simulating large impact crater formation in a layered or unlayered target. However, the physics of rock failure and deformation during crater collapse is still not understood (Melosh and Ivanov 1999). What is certain is that the effective cohesive strength of target rocks in an impact is orders of magnitude lower than that measured in the laboratory (Melosh 1977), and that the effective coefficient of friction is much lower than that of typical granular materials (McKinnon 1978). Suggested explanations for the apparent weakening of target materials during impact that were hotly debated at the first Bridging the Gap meeting include: acoustic fluidization (Melosh 1979), thermal softening (O'Keefe and Ahrens 1993, 1999), comminution (O'Keefe et al. 2001), and friction melting (Dence et al. 1977). No consensus was reached at that meeting, or since, but a recommended avenue for research to elucidate the mechanics of crater formation was a concerted effort to model and map mid-sized (15–30 km diameter) complex craters on Earth (Herrick and Pierazzo 2003). Such craters are large enough that their complex formation is clearly related to the formation of larger craters, and are small enough to be mapped, surveyed and simulated to a high level of detail (e.g., Osinski and Spray 2005; Wünnemann et al. 2005). Mid-sized complex craters are also sufficient in number that comparisons between craters can be made to better understand the effect of target properties on crater formation, and to establish which terrestrial examples are most representative of craters in that size range.

In this paper we compare observations and numerical models of three similar-sized (18–26 km diameter) terrestrial craters that formed in different target lithologies. The Ries and Haughton impact structures are two well-studied craters that formed in a mixed sedimentary and crystalline target. In contrast, El'gygytgyn is a well-preserved but less well-studied crater that occurred in a predominantly crystalline target. By comparing geological and geophysical observations at each crater we first demonstrate that all three craters are of similar size and, therefore, were likely formed by impacts of similar kinetic energy (i.e., within a factor of 2).

Given that the exact impact energy in each case is unknown, and that a major aim of our work is to quantify the effect of target variations on complex crater formation rather than reproduce observations at a specific crater, we chose to simulate the formation of each crater by numerically modelling impacts of the same kinetic energy into targets that represent the gross pre-impact target structure at each crater. By comparing the results from these simulations with observations we provide a simple quantitative model for mid-sized complex crater formation that can explain most of the observations at each crater. The combination of observations and modeling suggests that the major differences in the formation of El'gygytgyn, Ries and Haughton can be explained by the differences in thickness (or absence) of the pre-impact sedimentary layer in each target.

OBSERVATIONS

In this section we briefly summarize the observed structure of the three craters under investigation. A more detailed description of observations at each crater is given in subsequent sections. For more information, including geological cross sections of the pre-impact target lithology and structural interpretations based on geophysical data imaging the crater subsurface, see the references in the text.

Haughton

Location and Age

Haughton crater is situated on Devon Island in the Canadian Arctic Archipelago (75°22′N, 89°41′W). ^{40}Ar-^{39}Ar dating of potassic glasses yields an age of 39 ± 2 Ma (Sherlock et al. 2005) for the Haughton impact event. Since that time, Devon Island has remained tectonically stable, which in conjunction with the arid environment of the arctic desert has kept the crater well preserved (Osinski et al. 2005b). During annual expeditions since 1997, under the auspices of the multi-disciplinary Haughton Mars Project (Lee and Osinski 2005), Haughton has been studied extensively (for a summary see Osinski et al. 2005b) and mapped in detail (Osinski 2005): it is now one of the best studied impact craters on Earth.

Pre-Impact Target Structure

The pre-impact target sequence at Haughton comprises 1880 m of Lower Paleozoic sedimentary rocks, overlying Precambrian metamorphic basement rocks (Frisch and Thorsteinsson 1978; Thorsteinsson and Mayr 1987; Osinski et al. 2005b). The sedimentary layer consists of thick units of dolomite and limestone, with subordinate evaporite horizons and minor shales and sandstones (Thorsteinsson and Mayr 1987). The stratigraphic sequence dips gently to the west, exposing approximately north-south striking layers that are older to the east (Osinski and Spray 2005).

Crater Size

Erosion of the original crater rim complicates interpretation of Haughton's pristine morphology. At the present level of erosion the crater has an inner topographic depression ~16 km in diameter; the outer limit of this basin is marked by a semi-continuous ring of listric normal faults that record large (100–400 m) inward, and downward displacements (Osinski and Spray 2005). Concentric faults with strike lengths of many kilometers, but with meter-scale displacements, are present at a radius of 12 km in the north, west, and south, and 11 km in the east of the structure (Osinski and Spray 2005). The outermost concentric fault observed on a single seismic reflection line in the northwest, and the edge of the gravity-low is also at a radius of 12 km (Hajnal et al. 1988; Scott and Hajnal 1988). Consequently, the apparent crater diameter of Haughton is 23 km. Haughton exhibits a negative Bouger gravity anomaly 20–24 km in diameter with a maximum amplitude of −13 mgal (Pohl et al. 1988; Plescia 2005). The cause of the gravity low has been interpreted as a bowl-shaped zone with densities lower than the undisturbed surroundings (Pohl et al. 1988).

Ries

Location and Age

The Ries crater is located about 120 km northwest of Munich in southern Germany (48°53′N, 10°37′E). The amount of erosion of this complex impact structure is small due to a long period of shielding by post-impact sediments. Ries is the only exposed complex crater on Earth whose continuous ejecta blanket is largely preserved. New Ar-Ar laser probe dating of Ries tektites yield an age of 14.34 ± 0.08 Ma for the crater (Laurenzi et al. 2003). Since 1961, when Shoemaker and Chao (1961) proved its impact origin based on the discovery of coesite—a shock-induced high-pressure polymorph of quartz—Ries has become one of the most intensively studied craters on Earth. A comprehensive review of the Ries crater was published by (Pohl et al. 1977).

Pre-Impact Target Structure

The pre-impact target at Ries comprised a Triassic-Tertiary sequence of predominantly limestone, marl, claystone and sandstone that unconformably overlie Hercynian crystalline basement (Pohl et al. 1977) with subdued tilting. An east-west trending escarpment in the pre-impact landscape and fluctuations in strata thickness caused a sedimentary pile of 470 m in the north and 750 m in the south.

Summary of Crater Structure

Ries crater has an almost circular, relatively flat inner basin, 600–700 m deep and 12–13 km in diameter, that is entirely formed in crystalline basement. The inner crater is surrounded by a circular chain of crystalline hills standing about 50 m above the present basin. Outside this inner ring,

hummocky relief extends to the outer topographic crater rim with an approximate diameter of 24–26 km. The tectonic crater rim is defined by faults separating autochthonous from down-faulted parautochthonous strata that were identified by several geoelectric traverses (e.g., Hüttner et al. 1980; Hüttner 1988) and a seismic section across the rim (Angenheister and Pohl 1969) as well as field observation. Geophysical studies also suggest that impact-related subsidence of the basement may be confined to a radius of 10 km (Pohl et al. 1977). Ries exhibits a negative Bouger gravity anomaly ~20–24 km in diameter with a maximum amplitude of −18 mgal (Pohl et al. 1977). Ernstson and Pohl (1977) modeled this anomaly by a low-density, bowl-shaped zone 6 km deep, 22 km in diameter; the total mass deficit is estimated to be 70–100 Bt (Pohl et al. 1977).

El'gygytgyn

Location and Age

El'gygytgyn (pronounced el-j e-git'-gin) impact crater is located in central Chukotka, northeastern Russia (67°30′N, 172°34′E). An impact origin was confirmed by the discovery of shock-metamorphosed rocks, impact glasses and impact melt rocks (Gurov et al. 1978; Gurov and Gurova 1979). Recent ^{40}Ar-^{39}Ar dating of impact glasses has confirmed a crater age of 3.58 Ma (Layer 2000). El'gygytgyn is one of the best-preserved complex impact structures on Earth; despite erosion of the majority of the ejecta deposits, an uplifted topographic crater rim is still intact (Dietz and McHone 1976).

Pre-Impact Target Structure

The pre-impact target stratigraphy at El'gygytgyn is not well constrained due to limited exposure. The upper few hundred metres of the target comprises a sequence of siliceous volcanic rocks and tuffs of Late Cretaceous age (Feldman et al. 1981).

Summary of Crater Structure

El'gygytgyn has a rim-to-rim diameter (at the current level of erosion) of 18 km (Gurov et al. 2007). The majority of the interior of the crater is covered by Lake El'gygytgyn, which is about 12 km in diameter, centered about 3 km southeast of the crater center. A "weakly expressed" outer concentric ring with an average relief of 14 m is present at a radial distance of 15.5–16 km, although it is not clear what this represents and if this is a primary impact-generated feature (Gurov et al. 2007). El'gygytgyn exhibits a negative Bouger gravity anomaly 18 km in diameter with a maximum amplitude of −10 mgal (Dabija and Feldman 1982).

Summary Comparison

The El'gygytgyn, Ries and Haughton impacts occurred in areas of different target lithology. El'gygytgyn formed in a predominantly crystalline target; whereas, Ries and Haughton formed in a mixed sedimentary-crystalline target. The pre-impact sedimentary layer was ~1800–1900 m at Haughton and ~500–800 m at Ries. Thus, comparing observations at these craters may offer enlightening insight into the effect of sediment thickness on crater formation, provided that any such effect is not masked by the difference in scale of each event. In other words, the effect of sediment thickness on the formation these craters can be most reliably assessed if the impact energy was similar in each case. Impact energy is extremely difficult to estimate based on final crater morphology. Scaling laws have been established that relate transient crater size to impact energy with a reasonable degree of confidence. However, the size of the transient crater is not known with any certainty at any of these craters, thus our only recourse for comparing the impact energy released during each impact is to compare the present structural elements of each crater.

Comparing the "size" of El'gygytgyn, Ries and Haughton is complicated by the differences in preservation of each crater and the available observations. At Ries and Haughton the outermost major concentric normal fault is at 12–13 km radius. The weakly-expressed topographic high at 15.5–16 km radius observed at El'gygytgyn may be a comparable structural feature; however, the outermost concentric fault depends strongly on the properties of the near-surface rocks and may not be a good measure of crater size and, thus, of impact energy (Turtle et al. 2005). Detailed mapping is also required in order to identify such faults in eroded structures; in fresh craters these small-offset faults may be buried by the ejecta blanket. El'gygytgyn still possesses part of its uplifted rim, although much of its ejecta deposit has been eroded; it has a rim-to-rim diameter of 18 km. At Ries, in the southern and eastern part where erosion was less active than in the northern part, the top of the outermost concentric normal fault is still visible as a topographic rim, although whether this was also the location of the topographic rim in the pristine crater is unclear. Haughton has not retained any vestige of its uplifted topographic rim; hence, its pristine rim-to-rim diameter is more uncertain. It has been suggested that the major normal faults at ~8 km radius, which coincide with the edge of the topographic basin, provide a more appropriate estimate of the rim-to-rim diameter at Haughton than the outermost concentric faults (Osinski and Spray 2005). Geophysical studies of the Ries crater suggest that major impact-related subsidence, which includes displacement of the basement, may be confined to a radius of 10 km (Pohl et al. 1977). The −10 mgal gravity anomaly at El'gygytgyn is coincident with the rim-to-rim crater diameter, 18 km. The negative gravity anomalies at Haughton and Ries are similar in amplitude (−13, −18 mgal) and lateral extent (~10–12 km in radius) and may be more representative of the size of these events. Thus, despite some important structural differences,

Table 1. Summary of comparative dimensions of El'gygytgyn, Ries, and Haughton based on observations and model results.

	El'gygytgyn		Ries		Haughton	
Feature	Obs.	Model	Obs.	Model	Obs.	Model
Sediment thickness (m)	0	0	470–750	660	1800–1900	1800
Rim-to-rim diameter (km)	18[1]	19	?	20	?	20.8
Pre-impact surface diameter (km)	~15	16.8	?	17	?	17.5
Diameter of largest-offset concentric fault (km)	?	16	~22[2]	17.5	~16[3]	17
Apparent diameter (km)	31–32[4]	–	26[5]	–	23–24[5]	–
Transient crater diameter (km)	–	11	–	11.3	–	12.4
Rim height (m)	142[1]	175	?	176	?	190
Apparent depth[6] (m)	650	800	480–530	800	<200	800
Gravity anomaly diameter (km)	18[7]	–	20–22[8]	–	20–24[9]	–

[1]At current level of erosion.
[2]Estimate based on depression of basement and major fault at Thalmühle (this work).
[3]Estimate based on diameter of topographic depression and major semi-continuous listric normal fault (Osinski and Spray 2005).
[4]Diameter of outer rim: semi-continuous ring with ~14 m topographic relief (Gurov et al. 2007).
[5]Diameter of outermost concentric normal fault.
[6]Depth from current surface to top of syn-impact crater fill.
[7]Dabija and Feldman (1982).
[8]Pohl et al. (1977).
[9]Pohl et al. (1988); Plescia (2005).

El'gygytgyn, Ries and Haughton have similar dimensions when comparing the same structural observations (see Table 1) and hence it seems reasonable to assume that all three craters were formed by similar impact energies (i.e., within a factor of ~2).

Given the similarity of the inferred scale of the El'gygytgyn, Ries and Haughton impacts a logical starting point for numerical simulations of their formation was to assume that the impactor properties were the same in each case (i.e., constant impact energy). Obviously, this assumption implies that there are likely to be small discrepancies between the model results and geological observations for each crater, due to the difference between the actual and the assumed impact energy in each case. However, the assumption of identical impact energy in each impact allows us to compare more meaningfully the results of the three simulations with different sediment thicknesses, and to test the hypothesis that the differences in the internal crater structure at El'gygytgyn, Ries and Haughton can be explained by the different pre-impact targets at each crater.

NUMERICAL MODELING

Approach

To simulate the formation of Ries, Haughton and El'gygytgyn we used the iSALE shock physics code, or hydrocode, a multi-rheology, multi-material extension to the SALE (Amsden et al. 1980) hydrocode. To simulate hypervelocity impact processes in geologic materials SALE was modified by Boris Ivanov and Jay Melosh to include an elasto-plastic constitutive model, fragmentation models, various equations of state (EoS), and multiple materials (Melosh et al. 1992; Ivanov et al. 1997). iSALE includes all of these modifications plus further improvements to the strength model (Collins et al. 2004), multi-material modeling and, most recently, implementation of a porous compaction model (Wünnemann et al. 2006). The code is well tested against laboratory experiments at low and high strain-rates (Wünnemann et al. 2006) and other hydrocodes (Pierazzo et al. 2008). It has also been used in the previous numerical simulation of several terrestrial impacts: Chesapeake Bay (Collins and Wünnemann 2005), Ries (Wünnemann et al. 2005), Sierra Madera (Goldin et al. 2006), and Chicxulub (Collins et al. 2008). Moreover, the code was used to develop a generic, quantitative model for the formation of impact craters in crystalline targets (Wünnemann and Ivanov 2003).

To develop a simple, consistent model for the formation of the El'gygytgyn, Ries and Haughton impact craters, we simplified the target structure at each crater. In our models, the target consists of a crystalline basement below a sedimentary layer with a thickness of 1.8 km (Haughton), 0.66 km (Ries), and 0 km (El'gygytgyn), respectively. Further, based on the similarity in size of each structure, and to separate the effects of target properties from other variables, we assumed that each crater was formed by an impactor of the same size, composition and velocity. We held the impactor diameter (1.5 km), velocity (15 km/s) and composition (granite) constant and simulated impacts into one- and two-layered targets. Granite, with a density similar to that of a porous asteroid, was used to simulate the impactor for the convenience of reducing the number of different materials in the model. The projectile was resolved by at least 25 cells across its radius in all models. The angle of impact in all simulations was perpendicular to the target surface, enforced by the axisymmetric nature of the model. The assumption of vertical impact is unrealistic; moderately oblique impacts (40–50°) are six times more common than

near-normal incidence impacts (80–90°). However, the fact that for impact angles greater than ~15° to the horizontal all impact craters are circular in plan (Gault and Wedekind 1978; Bottke et al. 2000), suggests that the approximation of impact crater formation as an axisymmetric process is reasonable. We note that our model assumptions oversimplify the initial conditions of all three impacts. However, our aim is not to achieve a perfect match between models and observations; our primary focus is to quantify the effect of target lithology on mid-sized complex crater formation.

The thermodynamic behavior of each material in the model is described by an equation of state (EoS). We used tables generated using the Analytic EoS (ANEOS, (Thompson and Lauson 1972) for granite (Pierazzo et al. 1997) to represent crystalline basement rocks (and impactor) and the Tillotson EoS for limestone (Allen 1967) to represent the sedimentary sequence; as a comparison, we also used ANEOS tables for calcite (Pierazzo et al. 1998) to represent the sedimentary sequence. The atmosphere was not included in our models.

The most important aspect of impact models for properly simulating crater formation is the constitutive model. iSALE uses a constitutive model that accounts for changes in material shear strength that result from changes in pressure, temperature, and both shear and tensile damage (Melosh et al. 1992; Ivanov et al. 1997; Collins et al. 2004). For large impact crater formation, this must be supplemented by some form of transient target weakening model that facilitates deep-seated gravitational collapse of the initial bowl-shaped cavity (Melosh 1989; Melosh and Ivanov 1999). The physical explanation for this apparent target weakening is still a matter of debate; in our models the assumed explanation is acoustic fluidization (Melosh 1979). The effects of acoustic fluidization are incorporated into iSALE using the "block-model" (Melosh and Ivanov 1999; Ivanov and Artemieva 2002; Wünnemann and Ivanov 2003).

The preferred block-model and other strength model parameters for the uniform crystalline target (basement) in our simulations were based on those used in previous models of the Ries impact (Wünnemann et al. 2005), and lunar craters (Wünnemann and Ivanov 2003). Due to the wide variability in laboratory strength measurements for sedimentary rocks (e.g., Lockner 1995), we treated the strength model parameters of the sedimentary layer as free model parameters (within reason), which were assumed constant for the entire sedimentary sequence in each case. Through a series of model runs, we sought strength model parameters for the sedimentary layer that could explain observations at *both* Haughton and Ries impact structures. We note, however, that the Ries sediments include larger volumes of weaker rocks (e.g., marls and shales) than are present at Haughton. While not accounted for in this study, this may be important for refining simulations of each crater. All the important parameters for the models presented here are included in Table 2; the interested reader is referred to (Collins et al. 2004) for more detailed parameter definitions.

Table 2. Numerical model parameters.

Symbol	Definition	Value	
L	Impactor diameter (km)	1.5	
v_i	Impact velocity (km/s)	15	
ρ_i	Impactor density (kg/m^3)	2680	
T_{dec}	Decay time of acoustic vibrations (s)	30	
υ_{lim}	Kinematic viscosity of acoustically fluidized region (m^2/s)	375,000	
		Basement	Sediments
ρ	Reference density (kg/m^3)	2680	2700
Y_0	Cohesion (Yield strength at zero pressure; MPa)	50	50
Y_m	von Mises plastic limit (theoretical yield strength at infinite pressure; GPa)	2.5	0.65
μ_i	Coefficient of internal friction	1.5	2.0
Y_{d0}	Cohesion (initial damaged material; MPa)	15	15
μ_d	Coefficient of friction (damaged material)	0.6	0.4
T_m	Melt temperature (°K)	1673	1500
ξ	Thermal softening parameter	1.2	1.2
p_{bd}	Brittle-ductile transition pressure (GPa)	2.59	1.31
p_{bp}	Brittle-plastic transition pressure (GPa)	3.41	1.57

Modification to Strength Model

The strength model used in these simulations was the standard rock strength algorithm implemented in iSALE (Collins et al. 2004), with one modification. Collins et al. (2004) assumed that damaging the rock material in a cell reduced the strength at zero pressure (cohesion) to zero—effectively treating the damaged material as a granular material, such as sand. This assumption is good if the fracturing causing the damage is so pervasive that the resulting fragments are substantially smaller than the computational cell over which material properties are approximated. In circumstances where damage is the result of a single (or a few) fracture(s) through the cell, however, this assumption is an over-simplification; the rock mass will retain some cohesive strength. In other words, if the computational mesh is sufficiently fine to resolve the growth of individual fractures and shear zones then each cell of fully damaged material actually represents granular material in the fault and should have no cohesion. On the other hand, if the mesh is too coarse to resolve individual faults (which is the case in most large-crater impact simulations) then each "damaged" cell actually represents a mixture of large blocks

and small fragments, which should be assigned a cohesion parameterizing the effective cohesion of the rock mass. This parameterized cohesion is therefore dependent on mesh resolution.

Collins et al. (2004) illustrated the effect of mesh resolution on brittle failure. They compared the progressive brittle failure of two simulated blocks subjected to increasing strain; one block was resolved with a single cell, the other was resolved by a 100 × 100 mesh of cells. Total damage in the single-cell model was achieved at a strain of 5%; whereas, at the same strain in the high-resolution model several large blocks (clusters of undamaged cells) were separated by multiple fractures (thin zones of totally damaged cells), and pervasive fracturing was not achieved until the strain was greater than 10% (Collins et al. 2004, their Fig. 6). In this example, it is clearly inappropriate to treat the damaged material in the single-cell model as cohesionless at a strain of 5%. However, the example also illustrates that as a brittle material is exposed to increasing strain, after initial failure, fracture density increases and, hence, fragment size reduces by comminution. Therefore, after some amount of strain the maximum fragment size in an under-resolved rock mass will become small enough that the rock mass can be treated as a granular material, and the cell containing this material should lose its effective cohesion.

To account for the effective cohesion of a rock mass whose fractures are under-resolved, we supplemented the strength of the damaged material, Y_d, with a finite strength at zero pressure Y_{d0}. In addition, to include the effect of progressive failure of the brittle rock mass, and the reduction in fragment size with increasing strain, we degraded this cohesion with increasing strain. The most appropriate form for this relationship is still under investigation; in the present work, we defined the damaged material strength using:

$$Y_d = Y_{d0}(1-\varepsilon_*)^{0.25} + \mu_d p \quad \text{where } \varepsilon_* = \min\left(1, \frac{\varepsilon_p}{\varepsilon_g}\right). \quad (1)$$

In this equation, ε_p is the accumulated plastic strain, ε_g is the plastic strain at the point where cohesion is lost, and Y_{d0} is the cohesion of the unstrained damaged material. As in the original description of Collins et al. (2004), μ_d is the friction coefficient for the damaged material and p is the pressure. As discussed above, both ε_g and Y_{d0} will depend on mesh resolution; they should both increase with cell size, as fracture zones become increasingly under-resolved. However, the cohesive strength of many brittle materials is observed to decrease with increasing length-scale due to the increase in number and size of pre-existing weaknesses with sample size (e.g., Lockner 1995). Thus, the relationship between Y_{d0} and cell size is unclear at this stage. Observations at Haughton, Ries, and other similar-sized terrestrial craters, suggests typical block sizes of 0.1–1 km (Pohl et al. 1977; Ivanov et al. 1996; Osinski and Spray 2005; Kenkmann et al. 2006). Thus, at the resolution of our current simulations, with a minimum cell width of 25 m, fracturing of the target surrounding the crater is under-resolved and an effective cohesion is appropriate. In this work, the model parameters that gave the best results were ε_g = 0.3 and Y_{d0} = 15 MPa. Figure 1 illustrates the difference in total plastic strain at a point in time during numerical simulations of Haughton crater with and without the modification to the strength model described above. The cross sections are very similar in terms of large-scale deformation; however, the modified strength model causes localized deformation in the rim area as opposed to more distributed flow.

Lagrangian Tracer Particles

To simulate large deformation processes, such as impacts, iSALE uses a fixed computational grid and advects (moves) material through the grid. As a consequence, the provenance of material contained in a given grid cell changes during the simulation, and the state (pressure, temperature, etc.) of each grid cell at a given time represents only the state of that spatial location, and the material within it, at that time. To track the movement and thermodynamic history of "parcels" of material, information that would otherwise be lost, we use the widely employed strategy of Lagrangian tracer particles (tracers). These are massless particles that move with material flow without interacting with it and record the position and changing state of the material. In this work, we utilize the information recorded by tracer particles in two ways: to follow the deformation of layers of finer resolution than the lithologic layers in the models, and to record the peak shock pressure (e.g., Pierazzo et al. 1997) and total distance travelled of target material.

In our models, we represent each target with only two lithological units, sediments and crystalline basement. To visualize the deformation and final position of finer-scale layers within the sedimentary sequence, we color the tracer, or connect it to its neighbor with a line, based on its original position in the target sequence. It is important to note, therefore, that the deformation of these finer-scale layers does not reflect rheological variations between different sedimentary sequences in the model.

In this work, we also used tracers to quantify (as a function of radius) the provenance and shock history of material that most closely represents typical impact products that a geologist might identify in the field as an "allochthonous impactite." We refer to these tracers as "impactite tracers" in the following, which are divided into two categories: (1) crater-fill tracers are those impactite tracers that never leave the transient crater during crater formation; (2) ejecta-deposit tracers are those impactite tracers that are ejected ballistically from the *transient* crater. Note that this definition of the ejecta deposit is unconventional: it includes material that is ejected from the transient crater, but lands near the transient crater rim and is

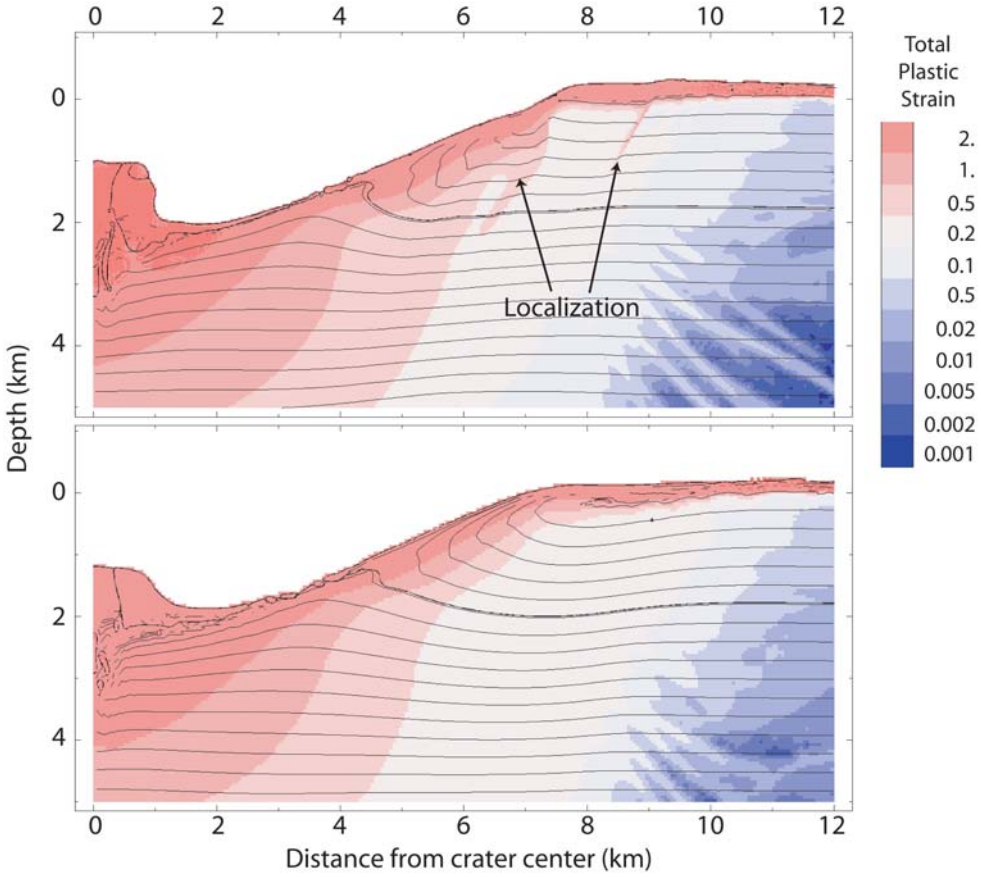

Fig. 1. A comparison of total plastic strain in the target at the same instant in time (55 s) for simulations of Haughton crater with (top) and without (bottom) the modification to the Collins et al. (2004) strength model described in the text. The modification produces localized deformation in the rim area during transient crater collapse.

subsequently transported inwards on top of the collapsing transient crater rim so that its final position is inside the *final* crater rim.

To distinguish impactite tracer particles that correspond to either crater-fill impactites or ejecta-deposit impactites we chose selection criteria based on analysis of the particle paths of each tracer particle in the model. The same criteria were used to select impactite tracers for the three modelled craters. A tracer was selected as a "crater-fill impactite" if it remained inside the crater throughout the simulation and if, at the time of transient crater formation (time = 20 s), its total path distance was greater than a specified distance (d_{cfi} = 3.5 km). In this case, the second criterion is a proxy for the amount of deformation (and comminution) that the tracer experienced and its proximity to the surface; in general, a greater distance travelled corresponds to a higher degree of deformation. Similarly, a tracer was selected as an "ejecta-deposit impactite" if its *initial* position was *inside* the transient crater and if, at the time of transient crater formation (time = 20 s), its total path distance was greater than a different specified distance (d_{edi} = 2 km). In this case, the second criterion is a proxy for ejection velocity; those tracers that travel further than 2 km in the first 20 seconds of crater growth are deemed to be part of the ejecta deposit. We note that distinguishing between ejected material and material that is merely uplifted near the transient crater rim in the model is ambiguous and that varying d_{edi} leads to a change in ejecta deposit thickness near the collapsed transient crater rim. We also note that both threshold distances apply only to craters with a transient crater ~12 km in diameter; we expect these distances to scale linearly with crater size, so that for a 6 km diameter transient crater the threshold distances will be half as large, but this has not been tested. To compute the thickness of impactite tracers as a function of radial distance the tracers were binned according to their final radial position. The total volume of tracers in each bin (each tracer is assigned a volume based on its initial position) was calculated and divided by the area of the bin to derive an average thickness.

The impactite tracer selection criteria, although somewhat arbitrary, allowed us to distinguish tracer particles that travelled large distances, experienced extreme deformation, and were deposited close to the final crater surface. Using different threshold distances (d_{cfi} and d_{edi}) for total tracer displacement changed the thickness of the impactite tracer layer, particularly near the collapsed transient crater rim. However, the choice of threshold

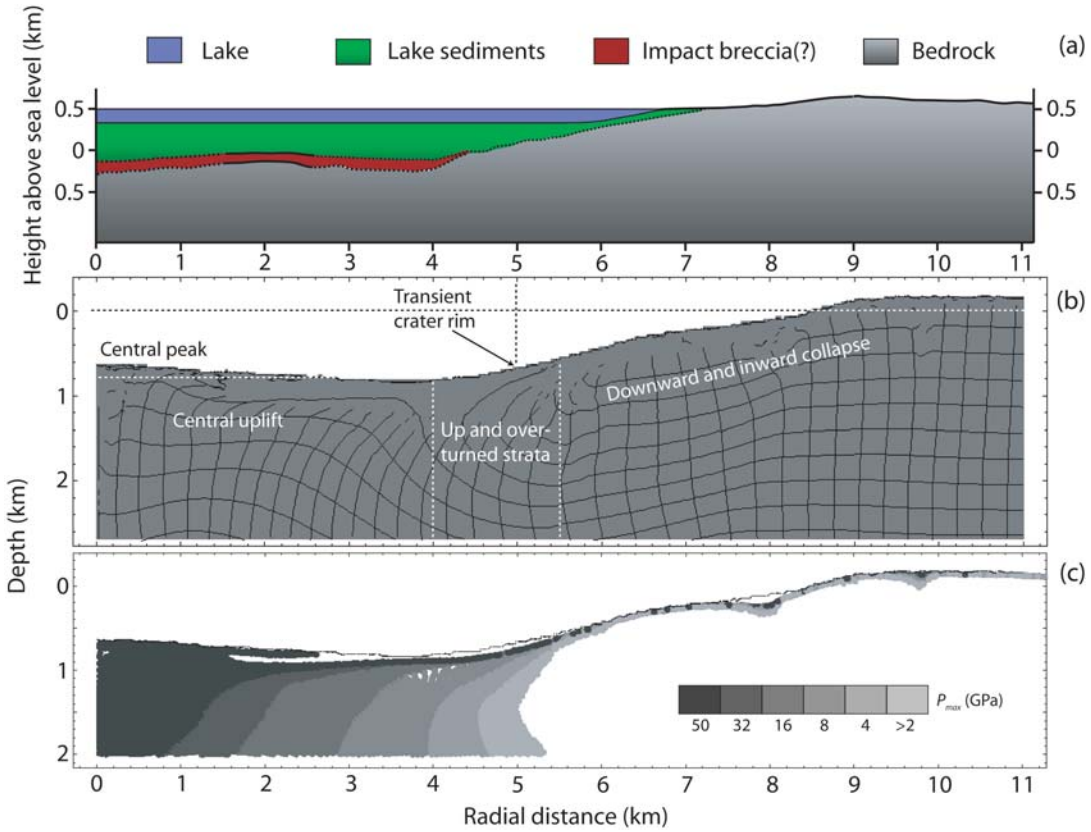

Fig. 2. A comparison between observation and model results for El'gygytgyn crater. a) Interpretive cross-section based on geologic observation and seismic surveys. b) Final model crater showing deformed grid of tracer lines. Tracers are only connected if their final separation is less than twice their original separation. c) Peak shock pressure distribution for tracer particles exposed to pressures greater than 2 GPa.

distance did not affect the general trend of peak shock pressure and provenance of impactite tracers as a function of distance. Thus, these criteria allow us to select tracer particles from the model that most closely represent the hundreds-of-meters-thick, highly brecciated crater fill and ejecta deposits observed at mid-sized complex craters. We emphasize, however, that the results afforded by this technique must be compared with observation with caution. In our models, the smallest volume represented by a tracer particle is ~8000 m^3, and this material is by definition homogeneous. The single peak shock pressure experienced by the tracer is therefore an average for this entire volume. In reality, small-scale heterogeneities within the material, such as fractures and pore-spaces, will affect shock propagation and produce a wide range of shock states about this approximate mean. In addition, our model does not simulate (accurately or at all) all the processes that allochthonous impactites will be exposed to during an impact, such as interaction with the atmosphere, devolatilization, turbulent mixing, ballistic sedimentation, pore-collapse, bulking, and so on. With these caveats, our impactite tracer results may be used to study general, large-scale trends in impactite provenance and shock state.

RESULTS

In this section, we present the results of our best-fit models of El'gygytgyn, Ries and Haughton craters, and interpretive geological cross-sections through each crater based on new and existing geological and geophysical data (Figs. 2, 4, and 6). A comparison of the time evolution of crater formation for each best-fit model is shown in Fig. 8. The observation-based cross sections for Ries and Haughton were constructed by T. K. and G. R. O. independently from the numerical models. They illustrate the large-scale structural observations that are most representative of radial profiles through each crater, to provide the most suitable comparison for the results of the numerical models. A summary comparison of crater dimensions based on models and observation is provided in Table 1.

Uniform Crystalline Target (El'gygytgyn)

Figure 2 shows a comparison between (a) inferred crater structure at El'gygytgyn from geologic and geophysical observations; (b) the final crater from our model of a 1.5 km diameter granite sphere impacting a granite half-space at

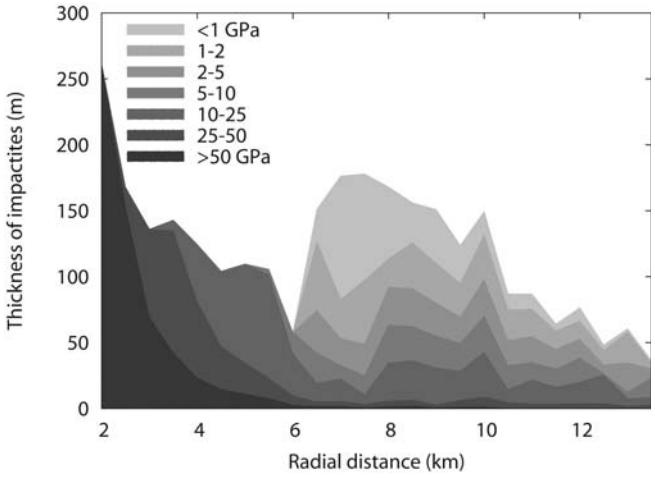

Fig. 3. Effective thickness of impactites exposed to different peak shock pressures as a function of final radial position from El'gygytgyn model. Based on the summed volume of tracer particles within a given radial interval that were selected as representing ejecta or crater-fill impactites and that experienced a given peak shock pressure. See text for more details.

15 km/s; and (c) the simulated distribution of target rocks shocked to a peak shock pressure greater than 2 GPa.

Observations

The majority of the morphometric observations of El'gygytgyn used in this work were derived from observations described by (Gurov et al. 2007); however, structural mapping at this crater has been limited by the paucity of outcrop, and the presence of a deep lake in the crater center. Post-impact lacustrine sediment terraces abut the lake to the west and north: together, the lake and the lacustrine terraces occupy almost the entire crater interior, covering a region ~15 km diameter. The water table is at an altitude of ~500 m, and the pre-impact surface has been inferred to be at ~600 m altitude (Gurov, personal communication). The remnant of the uplifted rim is well constrained by mapping; the average rim height is ~150 m above the assumed pre-impact surface, although at some azimuths the rim is entirely eroded by river valleys, and some peaks on the rim extend ~400 m above the lake. On average, the radius of the crater at the rim is 9 km; at the lake level the crater radius is 7.5 km. The rim has an asymmetric profile; the inner wall is steeper than the outer flank.

Seismic investigations over the lake suggest that the thickness of the post-impact lake sediments is ~400 m, and that the lake is ~150 m deep (Gebhardt et al. 2006). This implies an apparent crater depth of ~650 m (measured from the pre-impact surface to the top of the syn-impact crater fill) (Gurov et al. 2007). The observation of a 2 km wide positive anomaly (relative to the broader negative anomaly) of 2 mgal over the crater center was used to suggest the presence of a small central uplift (Dabija and Feldman 1982). A seismic reflection and refraction study (Gebhardt et al. 2006) suggests the existence of a broader central uplift and possible internal ring, although the central region of the crater was not well resolved by the refraction data set.

Model

The final modelled crater in Fig. 2b has a crater radius of 9.6 km measured at the rim and 8.4 km measured at the pre-impact surface. The rim height is ~200 m and the depth of the crater below the pre-impact surface is 800 m. A broad central peak, 200 m in height, is observed in the final crater; this collapsed from a maximum peak height of ~1 km (Fig. 8). The collapsed crater rim lies at a radial distance of ~5.5 km; inside this the crater surface is relatively flat. Beneath the crater, stratigraphic layers are down-dropped between a radial distance of 5.4 and 9 km, uplifted between the crater center and 4 km radius, and upturned or overturned in a transition zone in between.

Highly shocked (P_{max} > 50 GPa) and deformed material lines the crater floor to a depth of 100–200 m (Fig. 2c). There is also a hemispherical core of highly shocked material beneath the central uplift. Figure 3 shows that, overall, peak-shock pressures within the layer of impactite tracers decrease with radial distance. Inside 5.5 km radius, which corresponds to the final location of the inwardly collapsed transient crater rim, the impactite tracers all experienced peak shock pressures in excess of 5 GPa. Outside the final crater rim (10 km radius) the impactite tracer layer includes material exposed to a range of shock pressures, although very little that experienced a pressure >50 GPa. Beyond 10 km radius, the thickness of impactite tracers, and the relative amount of low shock material (<2 GPa), decreases with radius. In between 6 and 10 km radius, material exposed to the full range of peak shock pressures is included within the impactite tracers. This is material ejected at low velocity and late during excavation that is deposited near the transient crater rim. Notably, the relative amount of low-shock material (<2 GPa) is greatest within this zone, at a radius of ~7 km. A small, but significant, amount of material exposed to shock pressures greater than 50 GPa, which may induce melting, is also present in this zone.

Comparison

The lack of structural observations or drill cores at El'gygytgyn precludes a rigorous test of our numerical model of vertical impact in a purely crystalline target. The success of our model in simulating impacts in such targets was demonstrated previously (e.g., Wünnemann and Ivanov 2003). We include these model results primarily to provide comparison with numerical models of impacts in mixed sedimentary-crystalline targets, and in anticipation of upcoming drilling at El'gygytgyn. We also note that the presence of volcanic tuff layers in the upper target at El'gygytgyn, which were not included in our model, may affect the comparison between model results and observation.

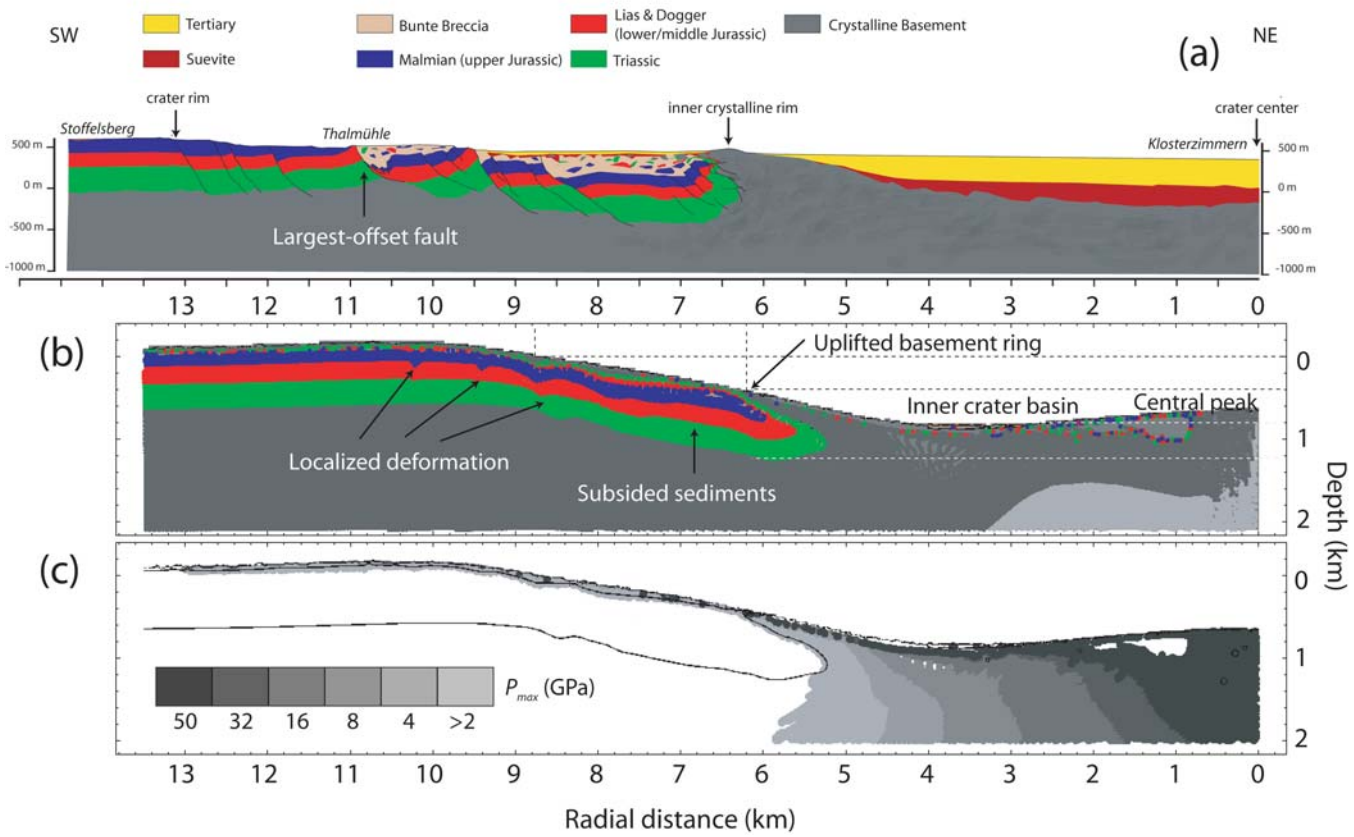

Fig. 4. A comparison between observation and model results for Ries crater. a) Interpretive cross section based on geologic observation and geophysical surveys (Ernstson 1974; Hüttner et al. 1980; Hüttner 1988). b) Final model crater showing tracer particles colored according to their original depth in the target. The colors correspond to different lithologies in the pre-impact target (blue—Malmian; red—Dogger; green—Triassic; grey—crystalline basement. c) Peak shock pressure distribution for tracer particles exposed to pressures greater than 2 GPa.

The simulated El'gygytgyn crater is ~200 m deeper than the inferred apparent crater depth based on observations (Gurov et al. 2007). A shallower simulated crater depth can be achieved by modifying the acoustic fluidization model parameters so that temporary weakening of material beneath the crater floor is more extreme or persists for longer. However, reducing the effective strength of the target also results in more substantial inward collapse of the transient crater rim, which leads to unrealistically shallow and wide crater walls and a wider crater. Instead, the depth discrepancy may be explained by the effect of dilatancy—the increase in volume (reduction in density) of materials undergoing brittle deformation (e.g., fracturing)—which is not currently considered by our numerical model. The effect of dilatancy on final crater morphology can be estimated using simple mechanical arguments (Artemieva et al. 2004). The 18 km diameter, −10 mgal Bouger gravity anomaly at El'gygytgyn implies a mass deficit of ~25 Bt (billion tons) beneath the crater floor. If this deficit is entirely due to dilatancy, and is assumed to be distributed uniformly beneath the ~5 km diameter crater floor, removing the associated void space would drop the crater surface by ~100–200 m.

Ries

Figure 4 shows a comparison between (a) inferred crater structure at Ries from geologic and geophysical observations; (b) the final crater from our model of a 1.5 km diameter granite sphere impacting a 660 m limestone layer above a granite half-space at 15 km/s; and (c) the simulated distribution of target rocks shocked to a peak shock pressure greater than 2 GPa. Colored tracer particles are used to illustrate the final position of target material in the model. The colors denote approximate parts of the sedimentary sequence at Ries for comparison with the observation-based cross section; they do not reflect rheological variations in the model.

Observations

The interpreted cross-section through Ries crater (Fig. 4a) is based on published geologic maps, geoelectric profiles (Ernstson 1974; Hüttner et al. 1980), and structural mapping studies (Hüttner 1988, Kenkmann, unpublished). The SW-NE profile runs from Schweindorf, southwest of the crater, to the approximate crater center, near Klosterzimmern,

and crossing Stoffelsberg near the town of Nördlingen. Profiles drawn through other azimuths of Ries would show qualitatively the same structural character as Fig. 4a, although the quantitative radial distances of the major features are variable.

Figure 4a shows an inner basin bounded by an uplifted ring of basement (inner ring) that now forms a topographic high; along the illustrated profile the inner ring crest has a radius of 6.5 km. At other azimuths, the inner ring has a minimum radius of 6.1 km (Wallerstein, W), 6.5 km (Wennenberg, SE) and a maximum radius of 7.1 km (Adlersberg, SW). The uplifted crystalline basement of the inner ring experienced severe brecciation and a shock metamorphic overprint. The outer limb of the inner ring shows overturning of the stratigraphic sequence, as was documented in the drill core at Wörnitzostheim (Dressler and Graup 1974; Pohl et al. 1977).

The near-surface crater structure, to about ~1 km depth, is well investigated. Under the post-impact sediments a layer of so-called "crater suevite" covers the crystalline basement. Suevite is a polymict breccia composed primarily of basement clasts, exhibiting a range of shock levels, with cogenetic impact melt clasts embedded in a particulate matrix that dominantly consists of unmelted particles (Stöffler and Grieve 2007). Drill cores and geoelectric measurements suggest that the inner basin has a depth of ~400 m from the top of the inner ring to the top of the syn-impact suevite deposits; the base of the suevite that is constrained by the drill core Forschungsbohrung Nördlingen 1973 is a further ~300 m below this level (Pohl et al. 1977). Relief of the post-impact surface inside the inner basin was suggested based on geoelectric measurements (Ernstson 1974).

Magnetotelluric measurements revealed an anomalously high electrical conductivity beneath the central structure of the crater, which was interpreted as resulting from a zone of brine-filled fractures to a depth of ~2 km (Wünnemann et al. 2005). This interpretation is consistent with a zone of reduced seismic P-wave velocities derived from seismic refraction profiles that extended 3–6 km below the surface (Angenheister and Pohl 1969; Pohl and Will 1974). Structural uplift beneath the crater of ~1 km was suggested, based on re-interpreted seismic refraction data across the crater (Wünnemann et al. 2005). The average P-wave velocity inside the crater and to a depth ~2.2 km below the surface is lower than that outside the crater; below this depth, however, the velocity inside the crater increases with depth in the same fashion as is observed at approximately 3.2 km depth outside the crater (Wünnemann et al. 2005).

Outside the inner ring is a broad zone of inwardly and downwardly displaced and heavily faulted sedimentary blocks, known as the megablock zone. This zone comprises both allochthonous blocks of brecciated crystalline and sedimentary rocks embedded in Bunte Breccia ejecta deposits, as well as parautochthonous sedimentary blocks that have slumped into the crater during crater collapse (Kenkmann and Ivanov 2006). Parautochthonous megablocks are less deformed in comparison to allochthonous megablocks. The megablock zone steps down from the present-day crater rim—the outermost concentric fault and topographic high—to a lower elevation just outside the inner ring. While fault zones are rarely directly exposed, their listrical shapes can be inferred from an antithetical rotation of the downfaulted blocks. Throws of faults were either deduced from geophysical profiles or from stratigraphic offsets. The least well defined data in the cross section are the 3 km outside the inner ring, where the inwardly collapsed sediments reach their greatest depth and are covered by allochthonous megablocks that are regarded as part of the ejecta blanket. In contrast to parautochthonous slump blocks, allochthonous megablocks are embedded in the ejecta. The top and base of the down-faulted sedimentary succession are not known here. The uppermost pre-impact sedimentary unit, the Malmian, outcrops at the surface at the crater rim but has been slightly eroded; we estimate that the top of the Malmian just outside the inner ring is approximately 300–350 m below the original exposure of the Malmian.

Draping the megablock zone is the ejecta deposit. The thickness of the ejecta layer amounts to several hundred metres just outside the inner ring and, in general, decreases with distance from the inner ring but is highly variable—deep pockets are common, such as inferred at Thalmühle (~10 km radius) based on geoelectric profiling (Hüttner et al. 1980, their profile 3). The ejecta deposit is primarily composed of Bunte Breccia deposits: clastic polymict breccias, whose constituents are mainly sedimentary rocks, with only 5–10% of crystalline rocks. The ratio of primary crater ejecta to local substrate components decreases with increasing radial range (Hörz et al. 1983) as more and more local material is incorporated by a process known as "ballistic erosion and sedimentation" (Oberbeck 1975). Patches of suevite, typically tens of metres-thick but up to 200 m in thickness, lie on top of the Bunte Breccia outside the inner crater (Pohl et al. 1977); whether they originally formed a continuous blanket on top of the Bunte Breccia is a matter of debate. The geochemical and petrographical composition of suevite suggests that it is predominantly derived from the crystalline basement of the Ries and experienced all stages of shock metamorphism. Larger blocks of crystalline ejecta reaching sizes of several hundred metres are common in the megablock zone (e.g., near Rudelstetten, ESE; Appetshofen, SE; Herkheim-Hürnheim, SSW; Utzmemingen, WSW; Wengenhausen-Marktoffingen NW), and increase in frequency with proximity to the inner ring. Several exposures of crystalline blocks can be found slightly offset from the cross section. According to other locations, 100 m of Bunte Breccia would be expected at the crater rim along the chosen cross section (Fig. 4a). This provides a rough estimate of erosion along the profile.

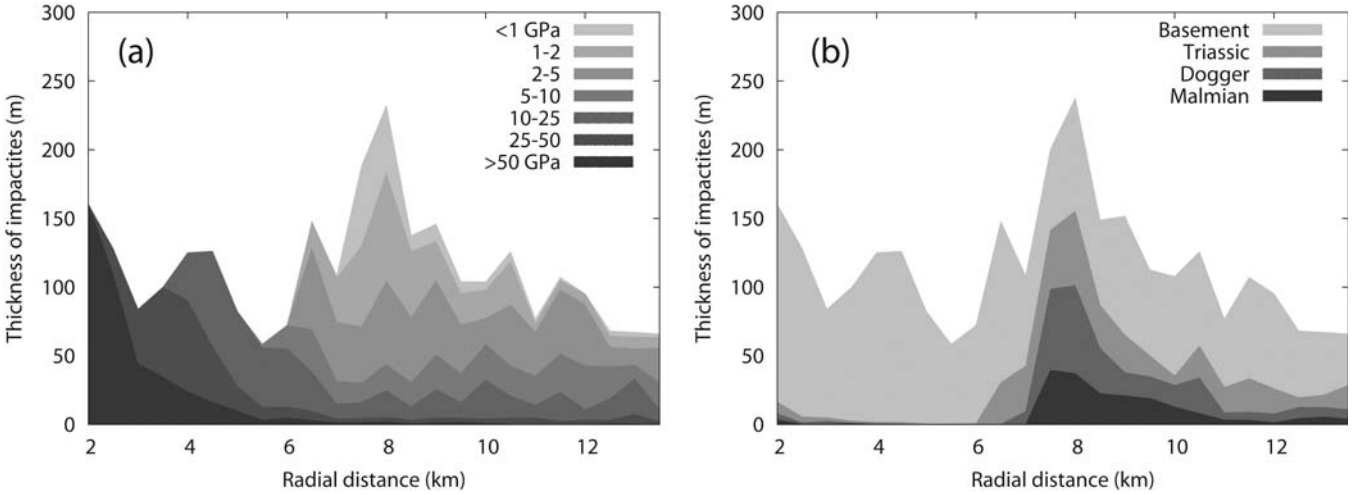

Fig. 5. Effective thickness of impactites from Ries model as a function of final radial position showing (a) peak shock pressure distribution and (b) provenance. Based on the summed volume of tracer particles within a given radial interval that were selected as representing ejecta or crater-fill impactites and that experienced a given peak shock pressure or were originally located at a given depth. See text for more details.

Model

Our numerical simulations of Ries crater are broadly consistent with previous models (Wünnemann et al. 2005). The final crater structure from our best Ries model (Fig. 4b) has an uplifted and overturned ring of basement rocks between a radius of 5.4 and 6.4 km. This represents basement material that is first uplifted and overturned to form the rim of the deep, bowl-shaped transient cavity, and which subsequently slumps inward and downward during crater collapse (Fig. 8). The bulk of the uplifted basement ring experienced a peak shock pressure of 2–4 GPa (Fig. 4c). Inside this uplifted basement ring, the crater surface is deeper with a maximum depth below the surface of 800 m; almost all sedimentary material within this inner basin has been removed. A central peak is also observed in our Ries models, ~200 m in height; this collapsed from a maximum peak height of ~1 km (Fig. 8). Beneath the inner crater, stratigraphic layers are uplifted by ~1 km. Some highly shocked (P_{max} > 50 GPa) material is situated in the ejecta deposit outside the uplifted basement ring, but the majority of this material lines the floor of the inner crater to a depth of 100–200 m.

In the Ries model, the uplifted basement ring is the innermost part of the continuous ejecta deposit. The ejecta deposit contains both basement and sedimentary material, which in the model remain distinct, with the stratigraphy inverted (basement ejecta overlying the sedimentary ejecta), in particular close to the uplifted basement ring (Fig. 4b). With radial distance from the inner ring the ejecta layer thins, and becomes increasingly sedimentary in composition. Figure 5 shows the peak shock pressure distribution and the provenance of "impactite tracers" as a function of radius. The relationship between peak shock pressure and radius (Fig. 5a) is qualitatively the same as for the El'gygytgyn model. Also evident from Fig. 5b is that inside the inner ring (<6 km radius) the impactite tracers include very little sedimentary material; whereas, outside the inner ring the impactite tracer layer is predominantly sedimentary in composition close to the inner ring.

Outside the uplifted basement ring, and underneath the ejecta deposit, is a zone of inwardly collapsed and subsided sediments. Depending on the strength model used for the sediments, the inward deformation can be localized, and extends to a maximum radius of 10–12 km. In the model shown in Fig. 4b, which uses the sedimentary strength model parameters in Table 2, localized deformation is observed at several radial distances between 8 and 10 km radius. The outermost evidence of inward displacement of the sediments is at ~9.5 km radius. Lowering the cohesion or friction coefficient of the damaged material increases the radial extent of inward deformation and changes the position of localized deformation, or suppresses it. The base of the sedimentary layer (top of the basement) has subsided ~400–500 m between 13 km radius and 6 km radius, beneath the uplifted basement ring. However, between 13 and 9 km radius the basement is uplifted ~50 m, so that significant basement subsidence is confined to a radial distance of ~10 km.

Comparison

The structural cross section and numerical model results for Ries are in good qualitative agreement. The major structural elements at Ries are reproduced by the model: the inwardly collapsed sedimentary megablock zone; the predominantly sedimentary ejecta deposit; the uplifted crystalline (inner) ring that is overturned in the outer limb; the deep inner basin filled by highly shocked material that may be interpreted as crater suevite. Moreover, the radial position of the uplifted crystalline ring, the depth of the inner basin relative to the inner ring, and the thickness of the ejecta deposit are all in reasonable quantitative agreement with observation. That the uplifted crystalline ring is now a

topographic feature at the Ries can reasonably be explained by differential erosion of the thick, ejecta deposit immediately outside the inner ring versus the more robust uplifted crystalline basement rocks. In addition, post-impact competent limestone reef bodies preferentially developed on top of the inner ring and protected them from further erosion. No detailed modal studies of ejecta between the inner ring and crater rim exist with which to test our model results. However, the modal make-up of the ejecta near the crater rim predicted by the model is dominated by basement material, whereas basement plays only a minor role in the field, even including the suevite (Gall et al. 1975). Partial erosion of basement material or a shallower excavation depth may explain this discrepancy between the model and observation.

Erosion at Ries complicates quantitative comparison of simulated crater morphology with observation. However, within the megablock zone abundant contacts between impactites and post-impact crater fill deposits occur at an altitude of 450–500 m, indicating relatively minor erosion. Assuming that the current level of erosion at Ries is not substantially below the level of the original pre-impact surface, the simulated final crater is ~200 m deeper than observation, as measured from the pre-impact surface to the top of the suevite (not the top of the basement). As with El'gygytgyn, we explain this discrepancy by dilatancy. The mass deficit beneath Ries crater is similar to that at El'gygytgyn, implying a very similar depth change if void space beneath the crater is removed.

The crater rim at Ries, defined as the outermost semi-continuous concentric normal fault, is ~3 km farther from the crater center than the outermost zone of localized deformation in the numerical model. In addition, the radial position of the uplifted basement ring is ~500 m farther from the crater center than the corresponding feature in the numerical model. Both these observations suggest that a closer match between model and observation may be obtained by using a larger impactor diameter or a higher velocity in the model. An alternative, or additional, explanation for the discrepancy between the position of the observed crater rim and the outermost inward deformation in the model is that the sedimentary layer at Ries was weaker than assumed in our model, or included weak horizons that expedited inward movement. Future work will investigate both these possibilities; our current model gave a good compromise between reproducing the major crater features at Ries and Haughton (see below) and demonstrated the effect of sedimentary layer thickness on crater formation, which were the main aims of this study.

Haughton

Figure 6 shows a comparison between (a) inferred crater structure at Haughton from geologic observations; (b) the final crater from our model of a 1.5 km diameter granite sphere impacting a 1800 m limestone layer above a granite half-space at 15 km/s, accounting for erosion of the crater rim; (c) as (b) but before erosion; and (d) the simulated distribution of target rocks shocked to a peak shock pressure greater than 2 GPa. Colored tracer particles are used to illustrate the final position of target material in the model. The colors denote approximate parts of the sedimentary sequence at Haughton for comparison with the observation-based cross section; they do not reflect rheological variations in the model.

Observations

The interpreted cross-section through Haughton crater (Fig. 6a) was drawn by G.R.O., based on detailed 1:10,000 to 1:25,000 scale structural geologic mapping of Haughton (Osinski 2005; Osinski and Spray 2005). Haughton exhibits azimuthal variations in crater structure and deformation. Figure 6a is a synthesis of structural cross sections at different azimuths around the crater, but is based most heavily on profiles AB and CH (Osinski and Spray 2005); it depicts a representative cross section that includes the main large-scale structural observations from the crater center outwards. Surface outcropping is well constrained for the majority of the profile due to excellent exposure along the transect. The geometry of deeper layers is constrained by detailed stratigraphic sections from just outside the crater and from comparisons with the seismic reflection profile (Scott and Hajnal 1988).

The radial cross-section through Haughton can be divided into three zones: the central uplift, surrounded by a complex collar zone, surrounded by an outer zone of down-faulted sedimentary rocks. The central uplift occupies the innermost ~6 km of the crater radius, and itself can be divided into three zones (Osinski and Spray 2005). The central region, inside ~1 km radius, is interpreted as a core of isolated, differentially uplifted megablocks. This core correlates with a positive magnetic anomaly and a small negative gravity anomaly. Surrounding the central core are km-scale coherent outcrops (or blocks) of Eleanor River Formation. These are internally faulted and are uplifted ~1 km from their pre-impact stratigraphic position. Overlying the uplifted blocks of Eleanor River Formation are several thin "plates" of Bay Fiord Formation strata.

The edge of the central uplift, between a radial distance of ~5 and ~6.5 km, is defined by a zone of sub-vertical and/or overturned strata. Depending on the sector, these strata comprise either Thumb Mountain, Bay Fiord or Lower Member Allen Bay formations. These lithologies are heavily fractured, faulted and are uplifted, on average, by ~200 m. Well-developed shatter cones are present in this zone, indicating shock pressures greater than 2 GPa. At a radial distance of ~6.5 km this intensely deformed ring of upturned strata transitions into an outer zone of large, less-deformed, down-dropped fault-bounded blocks, comprising different levels of the Allen Bay Formation. Inward and downward

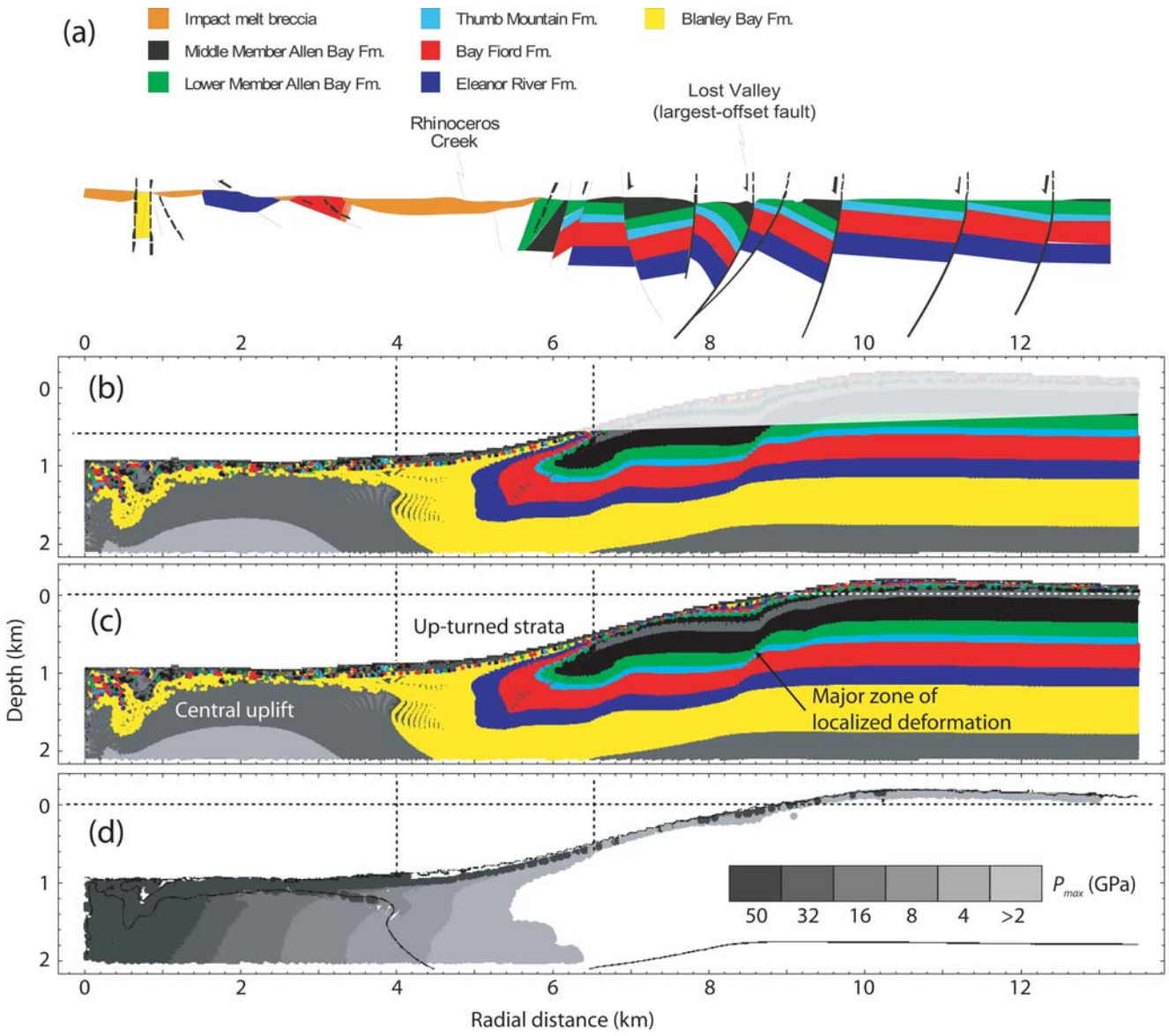

Fig. 6. A comparison between observation and model results for Haughton crater. a) Interpretive cross-section based on geologic observation. b) Final model crater accounting for erosion. c) Final model crater showing tracer particles colored according to their original depth in the target. The colors correspond to different lithologies in the pre-impact target. d) Peak shock pressure distribution for tracer particles exposed to pressures greater than 2 GPa.

deformation in this outermost zone is localized along major inward and outward dipping fault zones; consequently, down-dropped strata dip both inward and outward from the crater center. The most substantial fault displacements (~250–450 m) occur along an inward-dipping listric extensional fault at a radius of ~8–9 km. Several small-offset (<50 m) concentric normal faults occur between this major fault and the outermost semi-continuous fault at a radius of ~11 or 12 km, depending on the region of the crater, that defines the apparent crater rim.

Allochthonous crater-fill deposits form a virtually continuous 54 km^2 unit covering the central area of the structure (Redeker and Stöffler 1988; Osinski et al. 2005a). Analytical scanning electron microscopy (SEM) studies indicate that these rocks are carbonate-rich, clast-rich particulate impact melt rocks (Osinski and Spray 2001, 2003; Osinski et al. 2005a). The impact melt rocks have a maximum current thickness of ~125 m, and an estimated original thickness of ~200 m. Isolated outcrops up to a radial distance of ~6 km from the crater center suggest that the crater-fill originally completely occupied the central area of the crater.

Model

Our best-fit Haughton model has a diameter of 20.8 km measured at the topographic rim and a diameter of 17.5 km

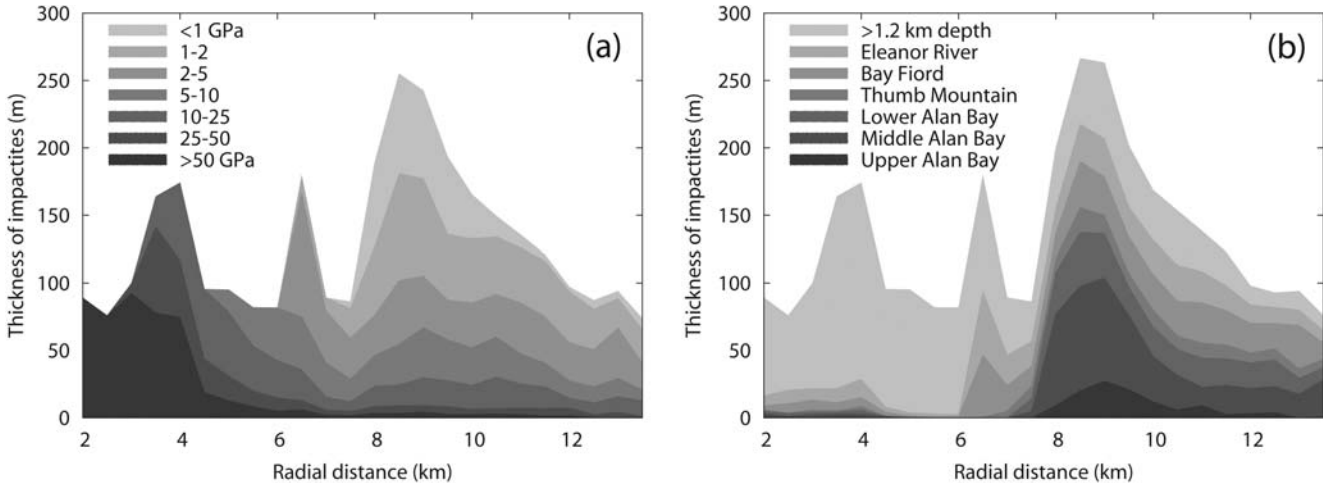

Fig. 7. Effective thickness of impactites from Haughton model as a function of final radial position showing (a) peak shock pressure distribution and (b) provenance. Based on the summed volume of tracer particles within a given radial interval that were selected as representing ejecta or crater-fill impactites and that experienced a given peak shock pressure or were originally located at a given depth. See text for more details.

measured at the pre-impact surface (Fig. 6c). The crater depth is 800 m below the pre-impact surface; the height of the rim above the pre-impact surface is 200 m. Immediately below the surface of the model crater, from the crater center out to beyond the rim, is a 100–200 m thick layer of highly deformed material. Figure 7 shows the peak shock pressure distribution and the provenance of "impactite tracers" within this layer as a function of radius. Compositionally, this material is a mixture of all parts of the sedimentary sequence. Inside ~6 km radius, this layer is material that remained inside the transient crater, lining the cavity during its growth and collapse; here, composition is primarily lower-sequence sediments (depth >1.2 km) with small amounts of upper sequence sediments (Fig. 7b). Outside 6 km radius the impactite tracer layer represents the continuous ejecta deposit, which covers the subsided transient crater rim, and forms positive topography at the crater rim and beyond. The ejected impactite tracers are primarily upper-sequence sediments (Allen Bay Formations; Fig. 7b). A range of peak shock pressures are experienced by the ejected impactite tracer material, including a small amount of material exposed to maximum pressures above 50 GPa (Fig. 7a). The impactite tracers inside 6-km, on the other hand, all experienced peak shock pressures above 5 GPa; the bulk of the impactite tracers within 4 km radius experience shock pressures greater than 50 GPa (Fig. 7a).

Underneath the highly shocked, highly deformed material just described, three structural zones can be identified in the final crater, analogous to the three zones observed at Haughton (Fig. 6c). Between the crater center and 4 km radius is an uplifted zone of lower-sequence sediments (yellow) above crystalline basement (grey). The basement is ~800 m higher in the central uplift relative to its position beneath the crater rim. Peak shock pressures in the uplifted basement decrease from >50 GPa at a radius of ~1 km to ~8 GPa at a radius of 4 km (Fig. 6d).

Between 4 and ~6 km radius is a zone of upturned, or overturned, sedimentary strata from the Bay Fiord, Eleanor River and Blanley Bay formations (Fig. 6c). This is material that formed the uplifted and overturned rim of the transient crater and subsequently collapsed into the crater (Fig. 8). The stratigraphic uplift of these strata decreases from 500 m to zero between 4 and ~6 km radius. Peak shock pressures of 2–4 GPa were experienced by the upturned and overturned material (Fig. 6d).

Beyond a radial distance of 6–6.5 km, and out to a radial distance of 10 km, the sediments below the ejecta deposit are subsided and dip gently toward the crater center (Fig. 6c). Downward displacements are accommodated along three inwardly dipping zones of localized deformation; the most significant of these is at a radial distance of 8.5 km and exhibits a vertical offset of ~300 m. Outside 10 km radius there is little deformation; net near-surface displacements are on the order of a few metres directed outward and upward (Fig. 8).

Comparison

Erosion at Haughton complicates the comparison of the final simulated crater with observation. We account for the effect of erosion on our model results, very approximately, by removing all ejecta and ~400 m of crater rim material outside 6 km radius (Fig. 6b). In addition, as at Ries and El'gygytgyn, dilatancy is expected to raise the floor of the modelled crater by ~200 m. Accounting for both these considerations is almost sufficient to reconcile the lack of significant relief now observed at Haughton; however, this estimate of erosion is higher than that suggested based on observations (<200 m average, Osinski et al. 2005b). Differential erosion may

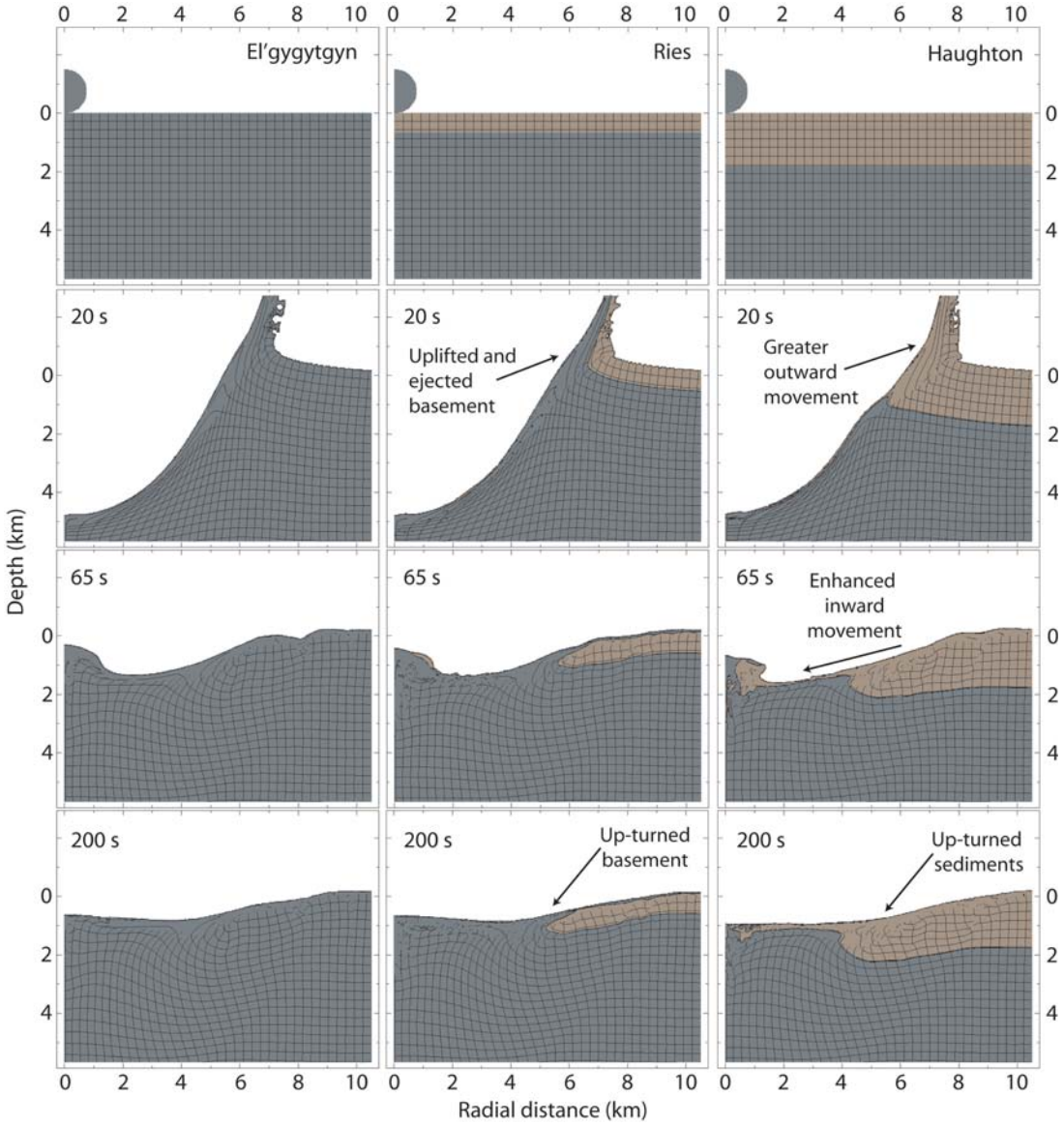

Fig. 8. A comparison of the temporal development of the simulated El'gygytgyn, Ries and Haughton craters. Shown are the times of transient crater formation (20 s); maximum height of central uplift (65 s); and final crater form (200 s). The Haughton and Ries models used two-layered targets. Grey represents crystalline material (granite); brown represents sedimentary material (limestone). Target deformation is illustrated by the grid of Lagrangian tracer lines. Tracers are only connected to form lines if their separation is less than twice their original separation.

explain the apparent discrepancy (e.g., some ejecta deposits are preserved in the south of the crater).

The final simulated Haughton crater, modified to account for erosion, displays the same key structural features as observed: the central uplift, covered in impact melt breccia; the outer zone of subsided sediments of the Allen Bay Formations; the complex zone of upturned and overturned strata surrounding the central uplift. In addition, the radial positions of the edge of the central uplift and zone of upturned strata (5–6.5 km) and the major localized inward deformation (8.5 km) are both in good quantitative agreement with observation, as is the estimated thickness of impact melt breccia and the estimated peak shock pressure at the edge of the central uplift (2–4 GPa). There are, however, some differences between modeling and observations, which are discussed below.

DISCUSSION

Overall, our best-fit crater models and the interpretive cross-sections based on geologic and geophysical observations are in good qualitative and, in some respects quantitative, agreement. In particular, the position and character of the major, well-constrained structural zones at both Ries and Haughton are successfully reproduced by the numerical models. This suggests that the assumption that

Haughton and Ries were formed by impacts of similar (i.e., within a factor of two) energy is reasonable and supports the hypothesis that the structural differences between them can be explained by the difference in sediment thickness in their respective pre-impact targets. There are, however, small but important general inconsistencies between the models and observation. In this section, we speculate on the cause of disagreement, and use the insight gleaned from our combined approach to infer the effect of sedimentary layer thickness on mid-sized complex crater formation.

Crater Depth

Different levels of erosion at the three craters studied complicates morphological comparison with numerical models. The pristine morphology of a mid-sized terrestrial crater is still uncertain. Our best-fit models do appear, however, to consistently overestimate the depth of the final crater, while at the same time reproducing the majority of other crater features. We suggest that the main reason for this is that the models do not consider dilatancy (bulking), which would increase the volume (decrease the density) of the deformed (fractured and sheared) target material beneath the crater, and raise the final crater floor (O'Keefe et al. 2001; Artemieva et al. 2004). An alternative, or additional, explanation for the deep model craters is that our models assume vertical impact. Based on the alignment of the Steinheim crater, the Ries and the fan-like tektite strewn field Stöffler et al. (2002) concluded that Ries and Steinheim were formed by oblique impact of a binary asteroid from WSW. Impacts that occur at an oblique angle to the target surface may create slightly shallower transient craters (as observed in experiments, Gault and Wedekind 1978) and collapse to form shallower final craters. As 3D numerical impact models develop it is hoped that these alternative explanations can be investigated.

Crater Diameter

Our results show that, for constant impact energy, both transient crater diameter and final crater diameter increase with increasing sediment layer thickness. The increase in transient crater diameter is about 5% for a 1.8 km sediment layer, compared to the uniform crystalline target; the increase in final crater diameter between the same two models is a further 5%. Thus, the increase in final crater size with increasing sedimentary layer thickness is due to both an increase in transient crater size and enhanced collapse in the sedimentary layer. However, the effect of the dry sedimentary layer on crater growth and collapse in the two cases simulated here is substantially less than the effect of water-saturated sediments observed in numerical simulations of the Mjølnir and Chesapeake Bay impacts (Shuvalov and Dypvik 2004; Collins and Wünnemann 2005). The final rim-to-rim crater diameter in our models increases from 19 km for the purely crystalline target impact (El'gygytgyn), to 20 km for a 660 m thick sedimentary layer (Ries) and 20.8 km for a 1800 m thick sedimentary layer (Haughton). Comparing these final simulated crater diameters with observation is not a trivial task, primarily due to erosion (e.g., Turtle et al. 2005). However, the structural comparisons made in the previous section suggest that our models are a close match for the scale of the El'gygytgyn and Haughton impacts, while the Ries crater may require a slightly larger impact energy than assumed in our model to better match observation.

An important consideration not included in our 2D models is the effect of lateral variations in target structure and three-dimensional deformation. Geological mapping shows that the Haughton and Ries impact structures, and their pre-impact targets, are markedly asymmetric. For example, Osinski and Spray (2005) showed that Haughton can be divided into six major structural sectors and that the tectonics of crater modification are manifest differently in each (e.g., intense faulting in the northern and eastern parts of structure). Thus, 3D numerical models are required to ascertain whether the results of our 2D models hold for the entire crater.

Central Peaks

Our models of Ries and El'gygytgyn both produce central peaks, which have not been recognized by observations. Central peaks are commonly observed in extraterrestrial impact craters, but are not always observed in terrestrial impact structures, even in well-preserved cases. Whether pristine terrestrial craters in predominantly crystalline targets always exhibit central peaks, and if not, why not, remain open questions. The crystalline basement beneath the crater suevite in the inner basin of the Ries was reached by one drill core only: the Forschungsbohrung Nördlingen 1973 (Pohl et al. 1977), which is situated 3.5 km away from the crater center. The transition from basement breccias to suevites does not produce a strong seismic reflection, in contrast to the contact between suevite and lake deposits that does (Angenheister and Pohl 1969). Thus a small central peak may exist at Ries that is disguised by a varying thickness of suevite. In agreement with observation (Osinski and Spray 2005), the simulated Haughton crater does not show a central peak. In the model, enhanced inward slumping of sediments on top of the central uplift during crater collapse suppressed the formation of a central topographic high (Fig. 8). This process was first suggested as a possible mechanism for the suppression of central peak formation in terrestrial craters based on observations at the 6 km diameter Decaturville impact structure (Offield and Pohn 1977).

Observations at Haughton of large coherent blocks of Eleanor River and Bay Fiord Formations in the central uplift may also suggest large-scale inward and upward collapse of deep-lying sediments (Osinski and Spray 2005). However, the presence of kilometer-scale outcrops of Eleanor River Formation strata within ~1–2 km of the crater centre is hard to reconcile with the modeling presented here. In the model, the only material present in the central uplift of the final crater

that was originally located at depths corresponding to the Eleanor River and Bay Fiord formations is highly shocked and heavily deformed (i.e., within the impact melt breccia). Based on knowledge of the target stratigraphy and mapping (Osinski 2005), we suggest that this large inwards movement was aided by two factors: the generation of weakness planes during excavation, and pre-existing weak horizons in the target. Detailed mapping at Haughton reveals several tectonic structures that were generated during the initial compressive outward-directed growth of the transient cavity (e.g., radial faults and fractures, bedding parallel detachment faults, and minor concentric faults and fractures, Osinski and Spray 2005). In addition, the sedimentary succession comprises several weaker sedimentary layers, in particular the evaporite-bearing Bay Fiord Formation. Together, these structural and lithological zones of weakness—which require much finer grid resolution to model—may have aided the large inward displacement of Eleanor River Formation strata.

An alternative explanation for the presence of large outcrops of Eleanor River Formation in the central uplift, is that the impact energy at Haughton was lower than in our models, so that the excavation depth was sufficiently shallow (~950 m) for large volumes of Eleanor River Formation to remain within the transient cavity. However, such shallow excavation would imply a much smaller transient cavity diameter than in our model, in which case the close agreement between the model and many of the other structural observations at Haughton would be lost.

Structure of a Mid-Sized Complex Crater

Observations at Ries and Haughton, combined with numerical models of these craters and El'gygytgyn, suggest that, broadly speaking, all three craters exhibit three main structural zones with increasing radial distance: a zone of structural uplift in the crater center; a collar zone of upturned and overturned, highly deformed strata; an outer zone of less-deformed inwardly and downwardly collapsed megablocks. Model results and observations suggest that the complex collar zone occupies radial distances between approximately 0.4 and 0.55–0.6 times the final crater radius *R* (i.e., 15–20% of the crater radius; measured to the pristine topographic crater rim). In this zone, the innermost strata are uplifted relative to their original position; the amount of uplift decreases with radius so that the outermost strata are down-dropped relative to their original position. The central uplift occupies approximately the central 40% of the crater; while the megablock zone occupies the outer 40–45% of the crater radius.

Collar Zone

Our models suggest the complex collar zone (0.4–0.6*R*) of mid-sized complex craters represents the collapsed transient crater rim. We suggest the presence of a topographic inner ring in this zone at Ries, and not at Haughton, is a consequence of the difference in sediment thickness. At Ries, stronger basement rocks are sufficiently close to the surface that they are uplifted and overturned during excavation and remain as an uplifted ring after modification and subsequent erosion of ejecta just outside the inner ring. This formation mechanism for the inner ring at Ries was first suggested by Pohl et al. (1977) and supported by previous numerical models of Ries (Wünnemann et al. 2005). At Haughton, the corresponding zone of the crater shows upturning and overturning of mid-sedimentary sequence strata. Overturned strata in the collar zone at Ries was documented in the Wörnitzostheim I drill core, 7.8 km SE from the crater center, where an inverted block of Jurassic to Triassic age is overlain by granite and suevite (Dressler and Graup 1974; Pohl et al. 1977).

Based on structural mapping, Osinski and Spray (2005) suggested that the zone of upturned strata at Haughton between 5 and 6 km may represent the uplifted and overturned rim of the transient crater that subsequently collapsed into the crater; however, their preferred explanation was that this structurally complicated region at Haughton represents the interference zone between an outward collapsing central uplift and inward collapsing crater walls. This was based on kinematic evidence that lithologies in this collar zone originally moved inwards, followed by later outward-directed displacement. Our numerical models do show late stage outward movement of the central uplift; hence, in reality this zone may represent both the original transient cavity rim and the focus of complex interactions between the central uplift and crater walls.

Allochthonous Impactites within the Final Crater

Observations at Haughton and Ries show a broad difference between the allochthonous impactites within the inner crater, which are predominantly comprised of deeply derived rocks (crater-fill impactites, Haughton; crater suevite, Ries), and those covering the megablock zone, which comprise a greater, or dominant, fraction of shallowly derived material (crater-rim impactites, Haughton; Bunte Breccia, crystalline ejecta, and surficial (fallout) suevite, Ries). To the extent that our models reproduce the emplacement of these impact products, this observation is consistent with our models; the "impactite tracers" that line the final crater interior show that the final location of the collapsed transient crater rim represents a transition in impactite tracer provenance, from deeply derived material inside the collapsed rim that never left the transient crater, to shallowly derived material outside the collapsed rim that was ejected from the transient crater. Thus, the change in provenance of allochthonous impactites with radial distance may help to establish the position of the collapsed transient crater rim at terrestrial mid-sized complex craters. In addition, Figs. 3, 5, and 7, illustrate that the impactite thickness outside the collapsed transient crater rim is maximum at ~7 km in the El'gygytgyn model, at 7.5–8 km at Ries, and at 8.5–9 km at Haughton, respectively. Thus, our model results suggest that for constant impact energy the radial position of the point of

maximum thickness of the continuous ejecta deposit that remains within the final crater rim increases with increasing sediment thickness.

In our models, the final location of the collapsed transient crater rim represents the divide between impactites that never left the transient crater and those that were ejected from the transient crater but landed within the final crater interior. In the models, the collapsed transient crater rim also represents a transition in impactite tracer shock state. The impactite tracers show higher average shock pressures, and a lower range of shock pressures, inside the transient crater rim than outside. This is in broad agreement with observation (see Osinski et al. [2008] for a detailed comparison of impactites at Ries and Haughton) and suggests that the main mass of the crater suevite remained in the transient cavity and was never airborne. However, our model does not adequately represent the formation and emplacement of these complex impact products, implying that our results must be compared cautiously with observation. In particular, the deposition of material subjected to shock compression at pressures above 50 GPa may be substantially different in reality from our model, as our equation of state for the sedimentary layer does not adequately describe the potentially important melting, decomposition, or vaporization processes, and we do not simulate the formation and settling of the hot ejecta plume. For example, the upper, graded parts of the crater suevite are almost certainly the deposits from a hot collapsing ejecta plume (Stöffler 1977), which was not simulated in our models. The enormous energy required to loft the entire volume of crater suevite almost vertically into the atmosphere for it to "fallback" into the inner crater precludes this as the sole emplacement mechanism for crater suevite, but whether the lower portion of the crater suevite was emplaced as a hot, turbulent gas-particle suspension (Pohl et al. 1977; Stöffler 1977) remains uncertain. Water vapor, formed explosively during impact, may have played an important role in the processing of impact products, but was not included in our simulations. It is possible that contact between water vapor entrained in the ejecta plume and hot impactites may have facilitated the formation of larger quantities of airborne suevite inside and outside the transient cavity than would be formed in a dry target. In addition, our models do not resolve the debate surrounding the emplacement of the surficial (or so-called "fallout") suevite outside the inner ring at Ries. More sophisticated, higher resolution models, which include multi-phase physics, combined with detailed geologic field work is required to resolve these complex issues.

SUMMARY

Our comparative observational and numerical modeling work supports the hypothesis that the El'gygytgyn, Ries and Haughton impact craters are similar in size, and that the structural differences between them are primarily due to the difference in thickness of the sedimentary cover. The presence of a topographic inner ring at Ries, and not at Haughton, appears to be a consequence of the difference in sediment thickness. At Ries, stronger basement rocks are sufficiently close to the surface that they are uplifted and overturned during excavation and remain as an uplifted ring after modification and subsequent erosion. At Haughton, the corresponding zone of the crater shows upturning and overturning of mid-sedimentary sequence strata. For constant impact energy, transient and final crater diameters increase with increasing sediment thickness.

By design, our models simplified the initial conditions of each impact studied, and assumed a constant impact energy. The slight mismatch between observation and model results at Ries may be resolved by using a slightly larger impact energy (larger impactor mass or velocity). Moreover, a closer quantitative match between all models and observation is likely to be achieved by the inclusion of several important factors not considered so far, such as (in estimated order of importance) more realistic target representation (improved material models, additional layers with rheologic contrasts, lateral layer thickness variations), dilatancy, localized deformation in three dimensions, enhanced resolution and non-vertical impact. Future modeling work will address these issues.

In agreement with observation-based models (Kenkmann et al. 2000; Kenkmann 2002; Osinski and Spray 2005), our work suggests that mid-sized (radius, R = 7.5–15 km, measured to topographic rim) complex craters comprise three structural zones: a zone of structural uplift in the crater center to a radial distance of ~0.4R; a collar zone of upturned and overturned, highly faulted strata between ~0.4R and ~0.6R; a zone of large, inwardly and downwardly collapsed megablocks between ~0.6R and R. The complex collar zone of these craters represents the collapsed transient crater rim; it may also be the focus of late stage interactions between the central uplift and crater walls. The layer of allochthonous impactites that cover the crater interior show a general, large-scale trend of decreasing shock state with radial distance. In addition, the final location of the collapsed transient crater rim represents a transition in impactite provenance and shock state, from deeply derived, highly shocked material inside the collapsed rim (crater-fill impactites), to shallowly derived material that exhibits a wider range of shock states—but on average lower—outside the collapsed rim (ejecta deposit within final crater interior).

Acknowledgments—We thank Boris Ivanov and Jay Melosh for their support in developing iSALE. We gratefully acknowledge Natalia Artemieva and Fred Hörz for their constructive reviews that improved this paper, and Richard Grieve for his helpful comments on an early version of this manuscript. This work was funded by NERC grant NE/B501871/1 and DFG grant WU 355/5-2.

Editorial Handling—Dr. Robert Herrick

REFERENCES

Allen R. T. 1967. *Equations of state of rocks and minerals*. Interim report to DASA under contract DA 49-146-XZ-462.

Amsden A. A., Ruppel H. M., and Hirt C. W. 1980. SALE: Simplified ALE Computer Program for Fluid Flow at all Speeds. 101 p.

Angenheister G. and Pohl J. 1969. Die seismischen Messungen im Ries von 1948–1969. *Geologica Bavarica* 61:304–326.

Artemieva N., Karp T., and Milkereit B. 2004. Investigating the Lake Bosumtwi impact structure: Insight from numerical modeling. *Geochemistry Geophysics Geosystems* 5, doi:10.1029/2004GC000733.

Bottke W. F., Love S. G., Tytell D., and Glotch T. 2000. Interpreting the elliptical crater populations on Mars, Venus, and the Moon. *Icarus* 145:108–121.

Collins G. S. and Wünnemann K. 2005. How big was the Chesapeake Bay impact? Insight from numerical modeling. *Geology* 33:925–928.

Collins G. S., Melosh H. J., and Ivanov B. A. 2004. Modeling damage and deformation in impact simulations. *Meteoritics & Planetary Science* 39:217–231.

Collins G. S., Melosh H. J., Morgan J. V., and Warner M. R. 2002. Hydrocode simulations of Chicxulub crater collapse and peak-ring formation. *Icarus* 157:24–33.

Collins G. S., Morgan J. V., Barton P., Christeson G. L., Gulick S., Urrutia-Fucugauchi J., Warner M. R., and Wünnemann K. 2008. Dynamic modeling suggests terrace zone asymmetry in the Chicxulub crater is caused by target heterogeneity. *Earth and Planetary Science Letters* 270:221–230.

Dabija A. I. and Feldman V. I. 1982. Geophysical characteristics of some astroblemes of USSR. *Meteoritika* 40:91–101.

Dence M. R., Grieve R. A. F., and Robertson P. B. 1977. Terrestrial impact structures: Principal characteristics and energy considerations. *Impact and explosion cratering*, edited by Roddy D. J., Pepin R. O., and Merrill R. B. New York: Pergamon Press. pp. 247–275.

Dietz R. S. and McHone J. F. 1976. El'gygytgyn: Probably the world's largest meteorite crater. *Geology* 4:391–392.

Dressler B. and Graup G. 1974. Gesteinskundliche Untersuchungen am Suevit der Bohrung Wörnitzostheim I im Nördlinger Ries. *Der Aufschluß* 25:404–411.

Ernstson K. 1974. Structure of Ries crater from geoelectric depth soundings. *Journal of Geophysics-Zeitschrift Fur Geophysik* 40: 639–659.

Ernstson K. and Pohl J. 1977. Neue Modelle zur Verteilung der Dichte und Geschwindigkeit im Ries-Krater. *Geologica Bavaria* 75:355–371.

Feldman V. I., Granovsky L. B., Kapustkina I. G., Karoteeva N. N., Sazanova L. V., and Dabija A. I. 1981. Meteorite crater El'gygytgyn. *Impactites*, edited by Marakhushev A. A. Moscow: Moscow State University Press. pp. 70–92.

Frisch T. and Thorsteinsson R. 1978. Haughton astrobleme: A mid-Cenozoic impact crater, Devon Island, Canadian Arctic Archipelago. *Arctic* 31:108–124.

Gall H., Müller D., and Stöffler D. 1975. Verteilung, Eigenschaften und Entstehung der Auswurfmassen des Impaktkraters Nördlinger Ries. *Geologische Rundschau* 64:915–947.

Gault D. E. and Wedekind J. 1978. Experimental studies of oblique impact. Proceedings, 9th Lunar and Planetary Science Conference. pp. 3843–3875.

Gault D. E., Quaide W. L., and Oberbeck V. R. 1968. Impact cratering mechanics and structures. *Shock metamorphism of natural materials*, edited by French B. M. and Short N. M. Baltimore, Maryland: Mono Book Corp. pp. 87–99.

Gebhardt A. C., Niessen F., and Kophsch C. 2006. Central ring structure identified in one of the world's best preserved impact craters. *Geology* 34:145–148.

Goldin T. J., Wünnemann K., Melosh H. J., and Collins G. S. 2006. Hydrocode modeling of the Sierra Madera impact structure. *Meteoritics & Planetary Science* 41:1947–1958.

Grieve R. A. F., Robertson P. B., and Dence M. R. 1981. Constraints on the formation of ring impact structures, based on terrestrial data. Multi-ring basins. Proceedings, 12th Lunar and Planetary Science Conference. pp. 37–57.

Gurov E. P. and Gurova E. P. 1979. Stages of shock metamorphism of volcanic rocks of siliceous composition—Examples from the El'gygytgyn crater (Chukotka). *Doklady Academii Nauk UkrSSR* 249:1197–1201. In Russian.

Gurov E. P., Koeberl C., and Yamnichenko A. 2007. El'gygytgyn impact crater, Russia: Structure, tectonics and morphology. *Meteoritics & Planetary Science* 42:307–319.

Gurov E. P., Valter A. A., Gurova E. P., and Serebrennikov A. I. 1978. Impact meteorite crater El'gygytgyn in Chukotka. *Doklady Academii Nauk UkrSSR* 240:1407–1410. In Russian.

Hajnal Z., Scott D., and Robertson P. B. 1988. Reflection study of the Haughton impact crater. *Journal of Geophysical Research* 93: 11,930–11,942.

Herrick R. R. and Pierazzo E. 2003. *Results of the Workshop on Impact Cratering: Bridging the Gap Between Modeling and Observations.* LPI Contribution 1162. Houston: Lunar and Planetary Institute. 156 p.

Hörz F., Ostertag R., and Rainey D. A. 1983. Bunte Breccia of the Ries: Continuous deposits of large impact craters. *Reviews of Geophysics and Space Physics* 21:1667–1725.

Hüttner R. 1988. Zum Bau des südlichen Ries-Kraterrandes. *Jahrbuch geologisches Landesamt Baden Württemberg* 30:231–251.

Hüttner R., Brost R., Homilius J., and Schmidt-Kaler H. 1980. Struktur des Ries-Krtsterrandes auf Grund geoelektrischer Tiefensondierungen. *Geologisches Jahrbuch* E19:95–117.

Ivanov B. A. 2005. Numerical modeling of the largest terrestrial meteorite craters. *Solar System Research* 39:381–409.

Ivanov B. A. and Deutsch A. 1999. Sudbury impact event: Cratering mechanics and thermal history. *Large meteorite impacts and planetary evolution II*, edited by Dessler B. and Grieve R. A. F. GSA Special Paper 339. Boulder: Geological Society of America. pp. 389–397.

Ivanov B. A. and Artemieva N. A. 2002. Numerical modeling of the formation of large impact craters. In *Catastrophic events and mass extinctions: Impact and beyond*, edited by Koeberl C. and MacLeod K. G. Boulder: Geological Society of America. pp. 619–630.

Ivanov B. A., Deniem D., and Neukum G. 1997. Implementation of dynamic strength models into 2D hydrocodes: Applications for atmospheric breakup and impact cratering. *International Journal of Impact Engineering* 20:411–430.

Ivanov B. A., Kocharyan G. G., Kostuchenko V. N., Kirjakov A. F., and Pevzner L. A. 1996. Puchezh-Katunki impact crater: Preliminary data on recovered core block structure (abstract). 27th Lunar and Planetary Science Conference. pp. 589–590.

Kenkmann T. 2002. Folding within seconds. *Geology* 30:231–234.

Kenkmann T. and Ivanov B. A. 2006. Thin-skin delamination around impact craters: An example from the Ries crater, Germany. *Earth and Planetary Science Letters* 252:15–29.

Kenkmann T., Ivanov B. A., and Stöffler D. 2000. Identification of ancient impact structures: Low-angle normal faults and related geological features of crater basements. *Impacts and the early Earth*, edited by Gilmour I. and Koeberl C. Berlin: SpringerVerlag. pp. 271–309.

Kenkmann T., Jahn A., and Wünnemann K. 2006. “Block size” in a complex impact crater inferred from the Upheaval Dome structure, Utah (abstract #1540). 37th Lunar and Planetary Science Conference. CD-ROM.

Laurenzi M. A., Bigazzi G., Balestrieri M. L., and Bouska V. 2003. $^{40}Ar/^{39}Ar$ laser probe dating of the Central European tektite-producing impact event. *Meteoritics & Planetary Science* 38: 887–893.

Layer P. W. 2000. Argon-40/Argon-39 age of the El’gygytgyn event, Chukotka, Russia. *Meteoritics & Planetary Science* 35:591–599.

Lee P. and Osinski G. R. 2005. The Haughton-Mars Project: Overview of science investigations at the Haughton impact structure and surrounding terrains, and relevance to planetary studies. *Meteoritics & Planetary Science* 40:1755–1758.

Lockner D. A. 1995. Rock failure. *Rock physics and phase relations: A handbook of physical constants*, edited by Ahrens T. J. WAshington, D.C.: American Geophysical Union. pp. 127–147.

McKinnon W. B. 1978. An investigation into the role of plastic failure in crater modification. Proceedings, 9th Lunar and Planetary Science Conference. pp. 3965–3973.

Melosh H. J. 1977. Crater modification by gravity: A mechanical analysis of slumping. *Impact and explosion cratering*, edited by Roddy D. J., Pepin R. O., and Merrill R. B. New York: Pergamon Press. pp. 1245–1260.

Melosh H. J. 1979. Acoustic fluidization: A new geologic process? *Journal of Geophysical Research* 84:7513–7520.

Melosh H. J. 1989. *Impact cratering: A geological process*. New York: Oxford University Press. 245 p.

Melosh H. J. and Ivanov B. A. 1999. Impact crater collapse. *Annual Reviews in Earth and Planetary Science* 27:385–415.

Melosh H. J., Ryan E. V., and Asphaug E. 1992. Dynamic fragmentation in impacts: Hydrocode simulation of laboratory impacts. *Journal of Geophysical Research* 97:14,735–14,759.

O’Keefe J. D. and Ahrens T. J. 1993. Planetary cratering mechanics. *Journal of Geophysical Research* 98:17,001–17,028.

O’Keefe J. D. and Ahrens T. J. 1999. Complex craters: Relationship of stratigraphy and rings to impact conditions. *Journal of Geophysical Research* 104:27,091–27,104.

O’Keefe J. D., Stewart S. T., Lainhart M. E., and Ahrens T. J. 2001. Damage and rock-volatile mixture effects on impact crater formation. *International Journal of Impact Engineering* 26:543–553.

Oberbeck V. R. 1975. The role of ballistic erosion and sedimentation in lunar stratigraphy. *Reviews of Geophysics and Space Physics* 13:337–362.

Oberbeck V. R. and Quaide W. L. 1967. Estimated thickness of a fragmental surface layer of Oceanus Procellarum. *Journal of Geophysical Research* 72:4697–4704.

Offield T. W. and Pohn H. A. 1977. Deformation at the Decaturville impact structure, Missouri. *Impact and explosion cratering*, edited by Roddy D. J., Pepin R. O., and Merrill R. B. New York: Pergamon Press. pp. 321–341.

Osinski G. R. 2005. Geological Map: Haughton impact structure, Devon Island, Nunavut, Canada. *Meteoritics & Planetary Science* 40(12).

Osinski G. R. and Spray J. G. 2001. Impact-generated carbonate melts: Evidence from the Haughton structure, Canada. *Earth and Planetary Science Letters* 194:17–29.

Osinski G. R. and Spray J. G. 2003. Evidence for the shock melting of sulfates from the Haughton impact structure, Arctic Canada. *Earth and Planetary Science Letters* 215:357–370.

Osinski G. R. and Spray J. G. 2005. Tectonics of complex crater formation as revealed by the Haughton impact structure, Devon Island, Canadian High Arctic. *Meteoritics & Planetary Science* 40:1813–1834.

Osinski G. R., Spray J. G., and Lee P. 2005a. Impactites of the Haughton impact structure, Devon Island, Canadian High Arctic. *Meteoritics & Planetary Science* 40:1789–1812.

Osinski G. R., Grieve R. A. F., Collins G. S., Marion C., and Sylvester P. 2008. The effect of target lithology on the products of impact melting. *Meteoritics & Planetary Science* 43. This issue.

Osinski G. R., Lee P., Spray J. G., Parnell J., Lim D. S. S., Bunch T. E., Cockell C. S., and Glass B. 2005b. Geological overview and cratering model for the Haughton impact structure, Devon Island, Canadian High Arctic. *Meteoritics & Planetary Science* 40:1759–1776.

Pierazzo E., Vickery A. M., and Melosh H. J. 1997. A reevaluation of impact melt production. *Icarus* 127:408–423.

Pierazzo E., Kring D. A., and Melosh H. J. 1998. Hydrocode simulation of the Chicxulub impact event and the production of climatically active gases. *Journal of Geophysical Research* 103: 28607–28625.

Pierazzo E., Artemieva N., Asphaug E., Baldwin E. C., Cazamias J., Coker R., Collins G. S., Crawford D., Elbeshausen D., Holsapple K. A., Housen K. R., Korycansky D. G., and Wünnemann K. 2008. Validation of numerical codes for impact and explosion cratering. *Meteoritics & Planetary Science* 43. This issue.

Plescia J. B. 2005. Haughton: A peak ringed impact structure (abstract #1303). 36th Lunar and Planetary Science Conference. CD-ROM.

Poag C. W., Hutchinson D. R., Colman S. M., and Lee M. W. 1999. Seismic expression of the Chesapeake Bay impact crater: Structural and morphologic refinements based on new seismic data. *Large meteorite impacts and planetary evolution II*, edited by Dressler B. O., and Sharpton V. L. Boulder: Geological Society of America. pp. 149–164.

Pohl J. and Will, M. 1974. Vergleich der Geschwindigkeitsmessungen im Bohrloch der Forschungsbohrung Nördlingen 1973 mit seismischen Tiefensondierungen innerhalb und außerhalb des Ries. *Geologica Bavarica* 72:75–80.

Pohl J., Eckstaller A., and Robertson P. B. 1988. Gravity and magnetic investigations in the Haughton Impact structure, Devon Island, Canada. *Meteoritics* 23:235–238.

Pohl J., Stöffler D., Gall H., and Ernston K. 1977. The Ries impact crater. *Impact and explosion cratering*, edited by Roddy D. J., Pepin R. O., and Merrill R. B. New York: Pergamon Press. pp. 343–404.

Redeker H. J. and Stöffler D. 1988. The allochthonous polymict breccia layer of the Haughton impact crater, Devon Island, Canada. *Meteoritics* 23:185–196.

Scott D. and Hajnal Z. 1988. Seismic signature of the Haughton structure. *Meteoritics* 23:239–247.

Senft L. E. and Stewart S. T. 2007. Modeling impact cratering in layered surfaces. *Journal of Geophysical Research* 112, doi: 10.1029/2007JE002894.

Senft L. E. and Stewart S. T. 2008. Impact crater formation in icy layered terrains on Mars. *Meteoritics & Planetary Science* 43. This issue.

Sherlock S. C., Kelley S. P., Parnell J., Green P., Lee P., Osinski G. R., and Cockell C. S. 2005. Re-evaluating the age of the Haughton impact event. *Meteoritics & Planetary Science* 40: 1777–1787.

Shoemaker E. M. and Chao E. C. T. 1961. New evidence for the impact origin of the Ries Basin, Bavaria, Germany. *Journal of Geophysical Research* 66:3371–3378.

Shuvalov V. and Dypvik H. 2004. Ejecta formation and crater development of the Mjølnir impact. *Meteoritics & Planetary Science* 39:467–479.

Shuvalov V., Dypvik H., and Tsikalas F. 2002. Numerical simulations of the Mjølnir marine impact crater. *Journal of Geophysical Research* 107:1-1–1-3.

Stöffler D. 1977. Research drilling Nördlingen 1973: Polymict

breccias, crater basement, and cratering model of the Ries impact structure. *Geologica Bavarica* 75:163–190.

Stöffler D. and Grieve R. A. F. 2007. Impactites, A proposal on behalf of the IUGS Subcommission on the Systematics of Metamorphic Rocks. In *Towards a unified nomenclature of metamorphic petrology.* IUGS Blackwell Publishers.

Stöffler D., Artemieva N. A., and Pierazzo E. 2002. Modeling the Ries-Steinheim impact event and the formation of the moldavite strewn field. *Meteoritics & Planetary Science* 37: 1893–1908.

Thompson S. L. and Lauson H. S. 1972. Improvements in the Chart D radiation-hydrodynamic CODE III: Revised analytic equation of state. 119 p.

Thorsteinsson R. and Mayr U. 1987. *The sedimentary rocks of Devon Island, Canadian Arctic Archipelago*. Geological Survey of Canada Memoir, vol. 411. Geological Survey of Canada. 182 p.

Tsikalas F., Gudlaugsson S. T., and Faleide J. I. 1998. The anatomy of a buried complex impact structure: The Mjølnir structure, Barents Sea. *Journal of Geophysical Research-Solid Earth* 103: 30,469–30,483.

Turtle E. P., Pierazzo E., Collins G. S., Osinski G. R., Melosh H. J., Morgan J. V., and Reimold W. U. 2005. Impact structures: What does crater diameter mean? *Large meteorite impacts III*, edited by Kenkmann T., Hörz F., and Deutsch A., GSA Special Paper 384. Boulder: Geological Society of America. pp. 1–24.

Wünnemann K. and Ivanov B. A. 2003. Numerical modelling of the impact crater depth-diameter dependence in an acoustically fluidized target. *Solar System Research* 51:831–845.

Wünnemann K., Morgan J. V., and Jödicke H. 2005. Is Ries crater typical for its size? An analysis based upon old and new geophysical data and numerical modeling. *Large meteorite impacts III*, Kenkmann T., Hörz F., and Deutsch A. GSA Special Paper 384. Boulder: Geological Society of America. pp. 67–83.

Wünnemann K., Collins G. S., and Melosh H. J. 2006. A strain-based porosity model for use in hydrocode simulations of impacts and implications for transient crater growth in porous targets. *Icarus* 180:514–527.